LOCAL STRUCTURE AND CHEMISTRY IN MARGINAL GLASS FORMING
ALLOYS

A THESIS SUBMITTED TO
THE GRADUATE SCHOOL OF NATURAL AND APPLIED SCIENCES
OF
MIDDLE EAST TECHNICAL UNIVERSITY

BY

TOLGA HAN ULUCAN

IN PARTIAL FULFILLMENT OF THE REQUIREMENTS
FOR
THE DEGREE OF MASTER OF SCIENCE
IN
METALLURGICAL AND MATERIALS ENGINEERING

SEPTEMBER 2020

Approval of the thesis:

LOCAL STRUCTURE AND CHEMISTRY IN MARGINAL GLASS FORMING ALLOYS

submitted by **TOLGA HAN ULUCAN** in partial fulfillment of the requirements for the degree of **Master of Science in Metallurgical and Materials Engineering Department, Middle East Technical University** by,

Prof. Dr. Halil Kalıpçılar
Dean, Graduate School of **Natural and Applied Sciences** _____

Prof. Dr. C. Hakan Gür
Head of Department, **Metallurgical and Materials Engineering** _____

Assoc. Prof. Dr. Y. Eren Kalay
Supervisor, **Metallurgical and Materials Engineering, METU** _____

Examining Committee Members:

Assoc. Prof. Dr. Benat Koçkar
Mechanical Engineering, Hacettepe University _____

Assoc. Prof. Dr. Y. Eren Kalay
Metallurgical and Materials Engineering, METU _____

Assoc. Prof. Dr. Caner Şimşir
Metallurgical and Materials Engineering, METU _____

Assoc. Prof. Dr. Sezer Özerinç
Mechanical Engineering, METU _____

Assist. Prof. Dr. Eda Aydoğan
Metallurgical and Materials Engineering, METU _____

Date: 03.09.2020

I hereby declare that all information in this document has been obtained and presented in accordance with academic rules and ethical conduct. I also declare that, as required by these rules and conduct, I have fully cited and referenced all material and results that are not original to this work.

Name, Surname: Tolga Han Ulucan

Signature   :

ABSTRACT

**LOCAL STRUCTURE AND CHEMISTRY IN MARGINAL GLASS
FORMING ALLOYS**

Ulucan, Tolga Han

M.S., Department of Metallurgical and Materials Engineering

Supervisor: Assoc. Prof. Dr. Y. Eren Kalay

September 2020, 71 pages

In this thesis structural and corresponding mechanical properties of marginal metallic glass-forming alloys were studied. $Al_{90}Tb_{10}$ system exhibits unique devitrification features due to their exceptional primary crystallization products of Al nanocrystals with populations reaching up to $10^{24}\,\mathrm{m}^{-3}$. A full agreement on how this abnormal nucleation event occurs is still lacking. Our previous studies on Al-RE (RE: rare-earth element) have shown that two different amorphous precursors prepared using melt-spinning and magnetron sputtering techniques showed clear differences in phase selection hierarchy upon continuous heating. It is considered that this difference is originated from the medium range ordered structure, exist in as-quenched melt-spun ribbon which is inherited from its molten state. In this study the local structure, chemistry and any possible higher order correlations were investigated by performing critical high energy synchrotron X-ray Diffraction (HEXRD),Extended X-ray Absoprtion Fine Structure (EXAFS), ab-initio and Reverse Monte Carlo (RMC) modelling. RE atoms were found to be highly correlated with Al atoms which results in formation of network dividing the amorphous matrix which in turn result in abnormal crystallization behavior. Afterwards, effects of these nanocrystals on mechanical properties are

investigated via micropillar compression tests and transmission electron microscopy (TEM). Embedding nanocrystals on amorphous matrix increased the fracture stress and ductility at the same time where as increasing heat treatment temperature beyond first crystallization event temperature caused formation of intermetallic compound which decreased the ductility while further increasing fracture stress.

ÖZ

METALİK CAM ALAŞIMLARINDA LOKAL VE KİMYASAL YAPI

Ulucan, Tolga Han

Yüksek Lisans, Metalurji ve Malzeme Mühendisliği Bölümü

Tez Yöneticisi: Doç. Dr. Y. Eren Kalay

Eylül 2020 , 71 sayfa

Marjinal metalik cam oluşturan alaşımlar yapısal ve mekanik olarak incelenmiştir. $Al_{90}Tb_{10}$ sisteminin kendine özgü devitrifikasyon özellikleri vardır. Bu özellikler sistemin ilk kristallenme reaksiyonu olan Al nanokristallerinin $10^{24}\,\mathrm{m}^{-3}$ popülasyonu ile oluşmasından kaynaklanır. Günümüze kadar bu anormal kristallenme reaksiyonunun nedeni konusunda uzlaşmaya varılamamıştır. Al-NTE (NTE=Nadir Toprak Elementleri) üzerine çalışmalarımızda iki farklı üretim yöntemi olan eriyik savurma ve manyetron saçılma yöntemleri ile üretilen aynı alaşımların faz seçilimi hiyerarşisinde farklılıklara rastlanmıştır. Bu farklılığın sıvı fazda olan orta erim düzeninden kaynaklandığı ve katı faza iletildiği düşünülmektedir. Bu çalışmada lokal yapıkimya ve üst seviye düzen ilintileri kritik sinkrotron X-ışını kırınımı, uzamış X-ışınları soğurumlu ince yapı, ab-initio ve reverse monte carlo modellemeleri ile incelenmiştir. NTE atomlarının Al atomları ile yüksek oranda ilintili olduğu ve bunun sonucunda bir ağ oluşturarak matrixi böldüğü gözlenmiştir. Sonrasında bu bölünmenin etkisiyle ortaya çıkan anormal seviyede yüksek sıklıkta oluşan naokristallerin mekanik özelliklere etkisi nanoçentik testleri ve transmisyon elektron mikroskopu ile incelenmiştir. İncelemenin sonunda matrixin kısmi kristallendirilmesinin kopma stresini ve aynı zamanda yumu-

şaklığı artırdığı gözlenirken ısıl işlem sıcaklığının artırılması ile oluşan metallerarası bileşiklerin kopma stresini artırmaya devam ederken yumuşaklığı düşürdüğü gözlenmiştir.

Anahtar Kelimeler: Metalik camlar, Nanokristaller, Kristallendirme, Sinkrotron X-ışını Kırınımı, Uzamış X-ışınları Soğurumlu Ince Yapı, Reverse Monte Carlo Simulasyonu, Mikrobasma testi, Geçirimli Elektron Mikroskopu

To my beloved family...

ACKNOWLEDGMENTS

TABLE OF CONTENTS

LIST OF TABLES

xiii

LIST OF FIGURES

xvi

LIST OF ABBREVIATIONS

2D	2 Dimensional
3D	3 Dimensional
$\lambda(k)$	Mean Free Path of Photoelectrons
APT	Atom Probe Tomography
BMG	Bulk Metallic Glass
CN	Coordination number
DSC	Differential Scanning Calorimetry
ECP	Efficient Cluster Packing
EDS	Electron Dispersive Spectroscopy
ETM	Early Transition Metals
EXAFS	Extended X-ray Absorption Fine Structure
f(k)	Elastic Scattering Probability
$f_i(Q)$	Atomic Scattering Factor
FCC	Face Centered Cubic
FEM	Fluctuation Electron Microscopy
GFA	Glass Formation Ability
HEXRD	High Energy X-ray Diffraction
HRTEM	High Resolution Transmission Electron Microscopy
$I_C(Q)$	Coherently Scattered X-ray Intensity
k	Wavenumber
LTM	Late Transition Metals
MRO	Medium Range Order
N	Degeneracy
PDF	Pair Distribution Function

R_i	Debye-Waller Factor
RE	Rare Earth
RMC	Reverse Monte Carlo
$S(Q)$	Total Structure Factor
S_0^2	Amplitude Reduction Factor
SAED	Selected Aread Electron Diffraction
TEM	Transmission Electron Microscopy
TM	Transition Metals
XAFS	X-ray Absorption Fine Structure
XRD	X-ray Diffraction

CHAPTER 1

INTRODUCTION

1.1 Amorphous Materials

Amorphous materials owing to their unique and superior properties coupled with their intriguing atomic structures have been a promising area of research especially with developments in characterization technologies. They have been widely used as conventional glasses to optical fibers, solar cells, batteries, polymers, thin films, implants and of course metallic glasses [1]. Unlike crystalline materials with long range ordered lattice structure; amorphous materials are highly disordered, does not have symmetry elements and contains only short to medium range order. Because of this characterizing, modeling and simulating these structures have required more sophisticated experimental and computational methods.

Over the course of last decades, amorphous materials have been developed and used as advanced engineering materials while some other systems are studied purely scientifically to better our understanding of nature. Despite their complicated production methods and size limitations metallic glass studies have improved our understanding of undercooling, nucleation, nanocrystallization and atomic structures.

1.2 Metallic Glasses

Metals and glasses are two of the oldest materials used by human kind as tools. First metal alloy bronze was discovered around 3500 BC in western asia [2]. Suprisingly first amorphous material used by humans is obsidian, a volcanic silicon dioxide glass used much earlier [3]. Amorphous and crystalline materials were then formed the

1

two main sub-classes of materials and studied separately. Until the first metallic glass was synthesized in 1960, an alloy of gold and silicon [4]. Since then there have tremendous amount of studies carried to synthesize, characterize and develop these materials [5–14]. Nowadays many alloy systems can be produced with amorphous structure that have excellent mechanical, electrical, magnetic and optical properties. The biggest obstacle standing between the metallic glasses to be used widely as engineering materials have been the production size [15]. Bulk metallic glasses mainly contain more abundant elements have been produced in mm size. Where as marginal metallic glasses due to requirement of much higher cooling rates have only been able to produced as thin films. Focus of this study will be on Al based marginal glass formers.

1.3 Al Based Marginal Metallic Glasses

Despite their low glass formation ability Al based metallic glasses have attracted much attention because of their high specific strength and light weight [16, 17]. In these alloys, Al is almost always accompanied by RE elements and sometimes transition metals (TM). First Al based marginal metallic glasses were synthesized at 1981 via melt spinning [18]. Al-(Fe,Co)-B system was followed by melt spun Al-Fe-Si [19] and Al-Si-Mn [20]. Despite achieving fully amorphous, mechanical properties obtained in these alloys were not satisfying. Brittleness was the main problem in most of the alloys in this class. Brittleness problem was overcome by the addition of IV-VI group transition metals (ETM), VII-VIII group transition metals (LTM) and rare earth elements [21–25] upon which Al-RE-TM have the highest glass forming ability. After these studies Al based marginal metallic glasses are considered for many engineering applications like coatings, medical goods, structural materials and sporting goods due to their high specific strength [26], ductility and corrosion resistance [27–29].

Marginal glass formers have a formation range beyond eutectic region unlike other metallic glasses and because of the strong covalent-like bonding between Al and RE, ETM, LTM elements (suppressing the formation of precipitates gets harder with stronger bonding) glass formation ability is relatively low [16, 30]. Although efforts to improve the glass formation ability (GFA) [31, 32] and developing methods to

2

study structure property relationships [33–35] were not fully successful they resulted in some empirical rules that enlighten the way.

Superior properties of marginal metallic glasses surely is a result of atomic packing and structural arrangements. However these advantages comes with unpredictable nature of these alloys. Empirical rules and structural models produced never achieved to apply all Al based metallic glasses [36]. Unlike bulk metallic glasses (BMG) they form glasses far from eutectic point [37]. Atomic size and composition rule generated for BMGs only apply for the latter part [36, 38]. Glass transition is not as apparent as BMGs [39]. Because of all these uncertainties study of Al based marginal metallic glasses heavily depend on revealing the true local atomic structure.

Computer simulations coupled with sophisticated experimental methods have a crucial role in understanding these structures. Some of these studies include the determination of composition range for AL-RE type metallic glasses as; $Al-Y_{9-13\%}$, $Al-La_{7-11\%}$, $Al-Ce_{7-11\%}$, $Al-Pr_{10\%}$, $Al-Nd_{8-12\%}$, $Al-Gd_{8-12\%}$, $Al-Sm_{8-16\%}$, $Al-Tb_{9-14\%}$ and $Al-Dy\&Ho\&Er\&Yb_{9-12\%}$ [22, 40]. RE element is the most crucial component due to their strong bond formation with Al, sluggish diffusion and very high atomic size mismatch [22, 41].
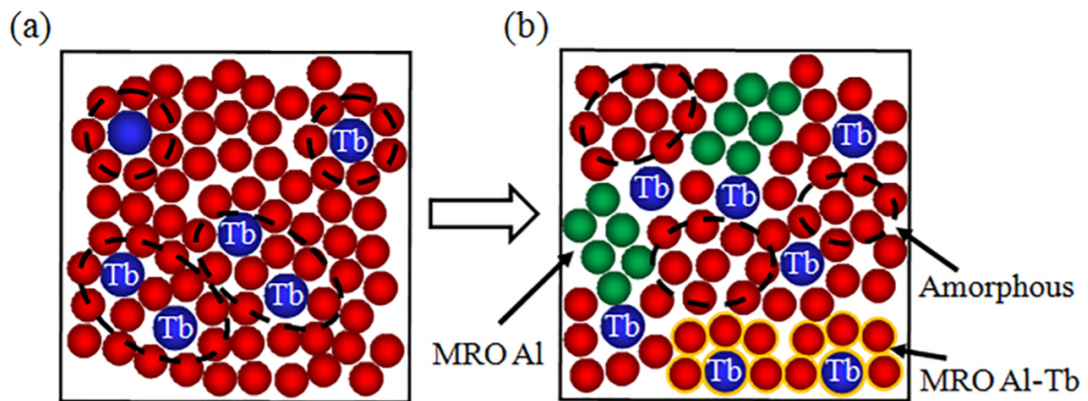
Figure 1.1: Schematics of $Al_{90}Tb_{10}$ system in (a) liquid and (b) as quenched state [17, 42].

Al-Sm system was heavily studied since it has the highest GFA. Atom probe tomography (APT), high resolution transmission electron microscopy (HRTEM) and reverse monte carlo (RMC) studies revealed that in as quenched alloy cooling rate

is high enough to bypass crystal formation and amorphous structure consists of Al surrounded Sm elements forming a network structure and Al rich regions given in [42–44]. Sm atoms in this structure seemed to form clusters where it takes 16 Al atoms around it as confirmed by XAFS studies [45]. Similar Al-Tb system was studied and it is stated that strong interactions between Al and Tb atoms divide the structure in to Al rich and Al depleted regions as given in Figure 1.1. Also liquid system was considered to be not as homogeneous as previously considered and the size of these Al rich regions are the main reason for high under cooling temperatures achieved in Al-RE systems [42].

Recently developed cluster alignment method was used to determine dominant short range order type in Al-Sm system [46, 47]. Dominating "3661" clusters are given in Figure 1.2.
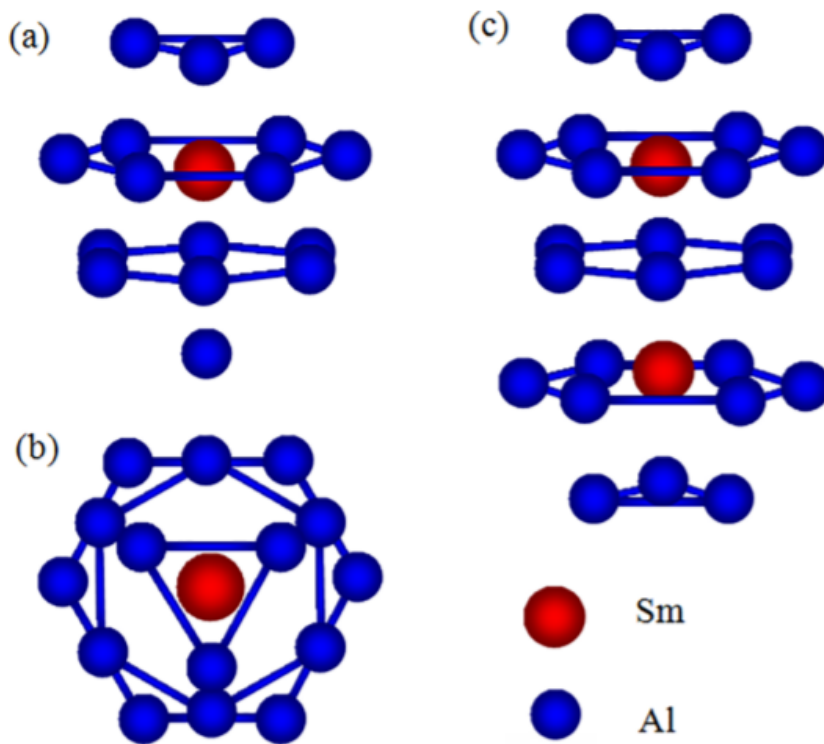
Figure 1.2: "3661" cluster in (a) front view, (b) top view and (c) two interpenetrating clusters in front view [46].

Al-RE-LTM metallic glasses have higher GFA than Al-ETM-LTM alloys and better packing efficiency than AL-RE alloys. Combined studies of neutron scattering,

HEXRD, HRTEM, EXAFS and computational methods structural features listed below were obtained [16] [17].

1. Al atoms surround the TM and RE atoms.

2. AL-TM bond is shorter than the sum of radii due to strong bonding via electron orbital hybridization.

3. Al and RE bond length is closer to sum of radii.

4. Disorder around RE is higher than TM

5. Icosahedral-like structures are observed in all Al based metallic glasses.

A model was proposed to define the SRO by use of solute centered clusters [48] however it fails to define the medium range order (MRO). Then efficient cluster packing model was developed to include the MRO [49, 50]. This model treats atoms as hard spheres and uses the packing principles as given in Figure 1.3 Later on Ef-
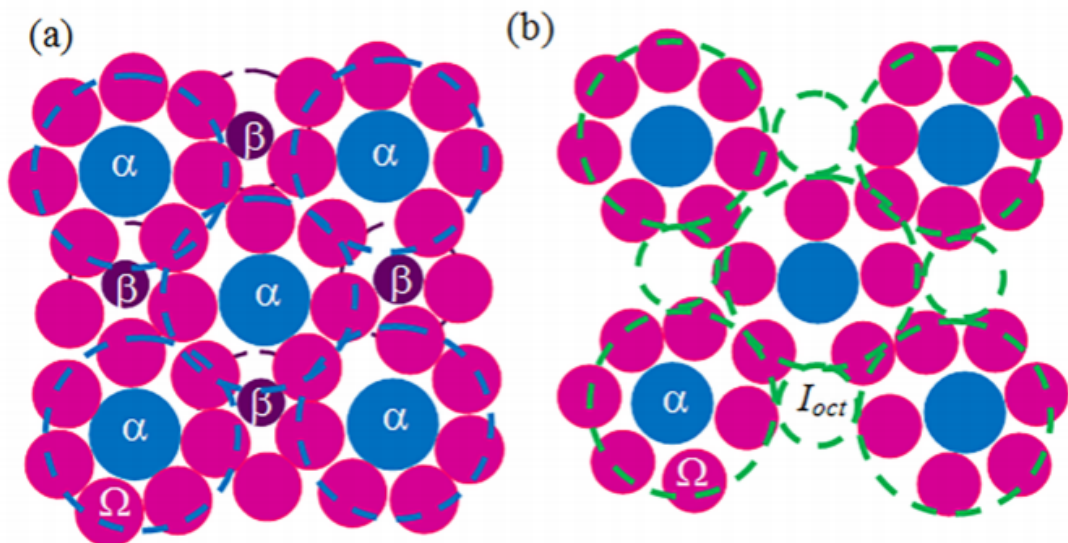
Figure 1.3: (a) ECP model and (b) Modified ECP model where α is the primary cluster former, β is the secondary solute, Ω is the solvent atom and I_{oct} is the octahedral interstitial site [49, 50].

ficient Cluster Packing (ECP) model was improved with electrochemical potential equalization principle and formed efficient atomic packing-chemistry coupled model

5

(EAPCC) [51]. This model is used to calculate the glass formation compositions for Al-RE-TM alloys. Where in $(Al_N - RE)TM_X$ N is the coorditaion number, X is the number of transition metal atoms. X is calculated by equalizing the chemical potential between RE and TM centered clusters. Based on this model another model was developed, icosahedral supercluster model, describing what kind of ineractions does clusters have.

$$(Al_N - RE)TM_x$$

$$x_{TM} = \left(\frac{r_{Al-RE}}{r_{Al-TM}}\right)^2$$

——— TM-centered clusters

——— RE-centered clusters

◯ — Al   ● — TM   ◯ — RE
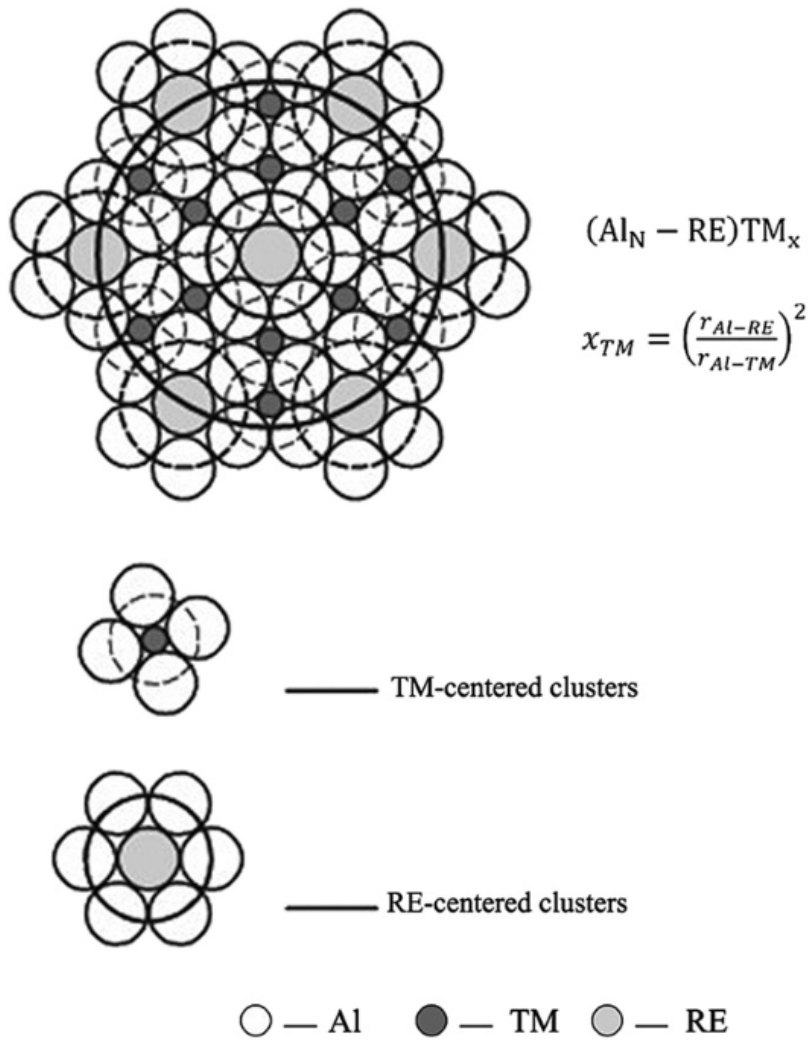
Figure 1.4: Efficient atomic packing-chemistry coupled model [51].

Al nanoparticle strengthened amorphous matrix alloys are of particular importance since they result in high specific strength and ductility [53–55]). Nanocrystallization in Al based marginal glass formers can be achieved via heat treatment, direct solid-

6
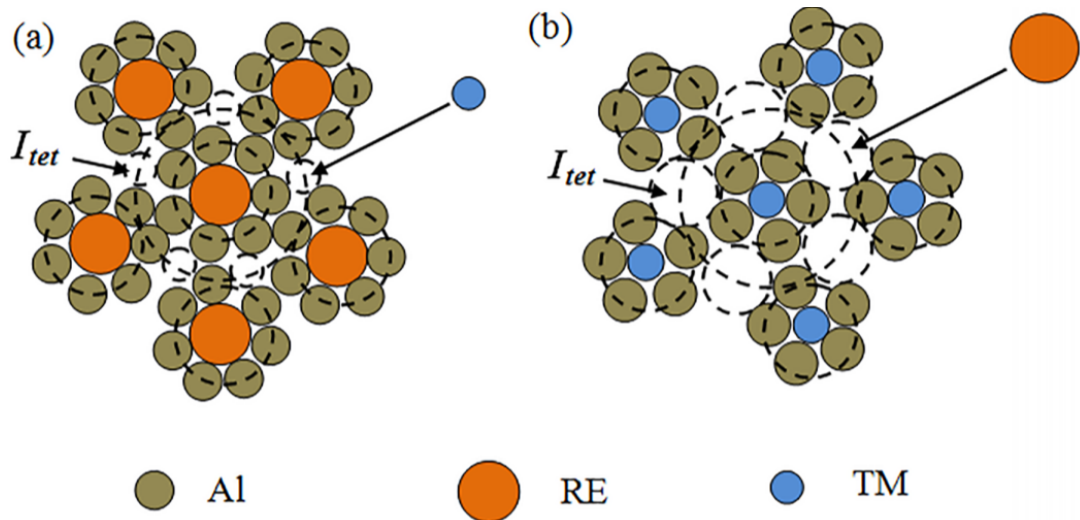
Figure 1.5: Icosahedral super cluster model for (a) TM atoms in tehrahedral sites and (b) RE atoms occupy tetrahedral sites [52].

ification, deformation or irradiation [56–60] There are various models proposed to explain the abnormal, high nucleation number density crystallization behavior and two of these models stand out. However there is still no clear and absolute agreement on it. This topic will be covered in the following chapters in detail.

1.4   Thermodynamics and Kinetics of Metallic Glasses

Metallic glasses combine the attributes of amorphous structure and metallic bonding. This is the main reason for their superior and unique properties. Obtaining amorphous structures in metallic systems is mainly done by rapid solidification where crystallization process is bypassed and amorphous structure is inherited from the parental liquid phase as given in Figure 1.6. In this section, glass formation and crystal formation was summarized.

Glass formation ability of a metallic system has been a heavily researched subject since it is the key to understand and develop metallic glasses. Glass formation ability can be assessed in terms of minimum cooling rate required to keep amorphous liquid phase from nucleation during solidification. In other words crystal nose given in Figure 1.6 should be on the far right side while provided cooling rate must be as
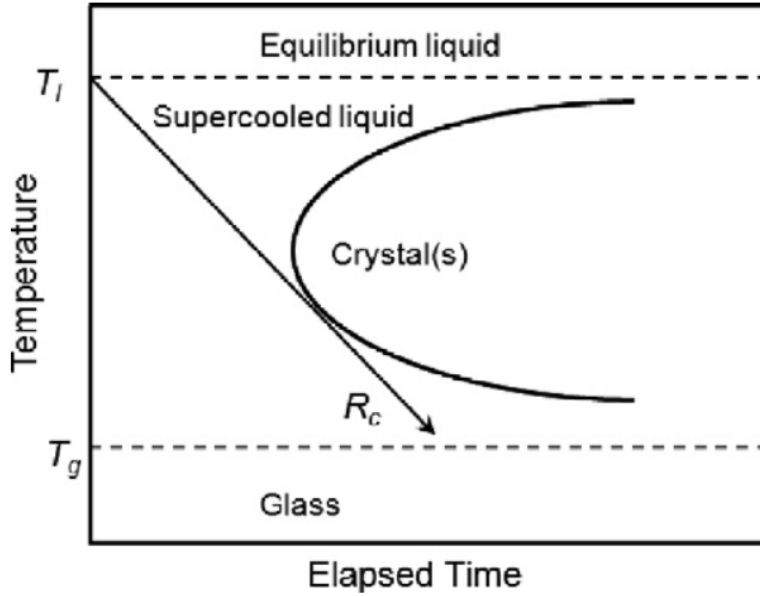
Figure 1.6: TTT diagram of a liquid bypassing crystal formation with critical cooling rate of R_c [1].

steep as possible to avoid crystal formation [61, 62]. Although many parameters affect the glass formation ability, there are empirical rules established over the years: (i) constituent element number must be three or higher, (ii) heats of mixing between constituent elements must be negative and (iii) significant atomic size ratio difference (about 12%). Mechanisms of how these rules improve the stabilization of liquid state and glass formation is given in Figure 1.7 [8, 63]. These rules are based on the "confusion principle" which is a phenomenon later used in high entropy alloys as "cocktail effect". In both phenomenon if complexity of a system increases it is harder to form unwanted crystals from a high number of choices so system tends to form amorphous or disordered structures [64]. Marginal metallic glasses on the other hand have a lower glass formation ability. These systems can only form glasses at distinct composition ranges and require much higher cooling rates. Bulk metallic require cooling rates of $10^3 - 10^2 \, \mathrm{K \, s^{-1}}$ whereas marginal metallic glasses require $10^5 - 10^6$ $\mathrm{K \, s^{-1}}$. While these mainly thermodynamic rules act as crucial guidelines, kinetic parameters are also equally important. Glass transition kinetics are highly dependent on specific volume and viscosity [65]. During cooling a molten material its specific volume decreases due to thermal shrinking. If a material goes through crystallization this

8

The constituent elements more than three kinds with large atomic size ratios above 12 % and negative heats of mixing

Increase in the degree of dense random packed structure
(topological and chemical points of view)

Formation of liquid with new atomic configurations and multicomponent interactions on a short-range scale

| **Increase of solid/liquid interfacial energy** | **Difficulty of atomic rearrangement** $\left(\begin{array}{c}\text{decrease of atomic diffusivity,}\\ \text{increase of viscosity}\end{array}\right)$ | **Necessity of atomic rearrangement on a long-range scale for crystallization** |

Suppression of nucleation of a crystalline phase   **Increase of T_g**   **Suppression of growth of a crystalline phase**

Decrease of T_m, Increase of T_g/T_m

Figure 1.7: Liquid stabilization and glass formation ability mechanisms for bulk metallic glasses [8].

change in volume is sudden and at a constant temperature due to drastic atomic arrangement changes. However if crystallization is bypassed specific volume continues to decrease until glass transition temperature at which viscosity increases and liquid solidifies with amorphous structure. Amorphous structure is preserved due to very limited atomic movements that is required for crystal formation. This phenomenon is shown in Figure 1.8.

1.5   Structure of Metallic Glasses

Unlike crystalline materials, structural analysis of amorphous materials is not straight forward. Crystalline systems are well defined in their atomic positions, symmetry elements and defects. However in amorphous materials, exact structure is neither necessary nor feasible to extract. Defining key features between the atoms and extracting main interactions statistically can reveal the structure property relations and glass formation phenomena. There are many parameters and methods developed for
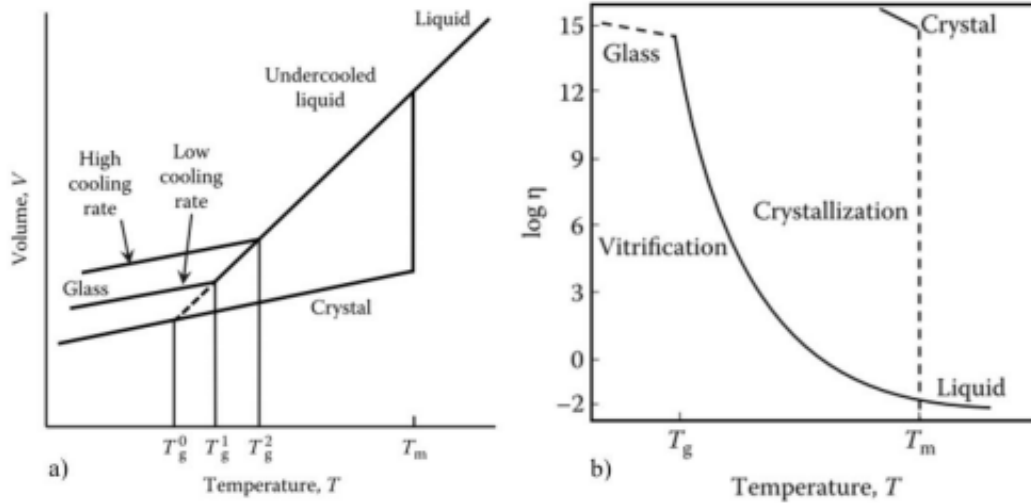
Figure 1.8: specific volume change (a) and accompanied viscosity change with respect to temperature in crystals and glasses [1].

this purpose. Most of these are mainly aimed to reveal short to medium range order and structural patterns [1, 16, 66–68].

1.5.1 Structure Factor, Pair Distribution Function and EXAFS

Structure factor $S(Q)$ have similar but different names for crystallographers and in the society of amorphous materials. $S(Q)$ is referred to as structure factor which is a function of diffraction vector defined in reciprocal space that represents total scattering intensity for amorphous materials society. This function covers the scattering events of Bragg peaks, elastic and inelastic scattering. Crystallographers however use the name structure factor to represent F_{hkl}. In this study nomenclature of amorphous materials society is preferred. Pair distribution function on the other hand is a probability function of finding atomic pairs as distance from an average atom. It contains information about all the atomic pairs in the structure and not limited certain elements. Pair distribution function of a sinlge pair can be represented by Equation (1.1)

$$g_{\alpha\beta}(r) = \frac{N}{4\pi r^2 \rho N_\alpha N_\beta} \sum_{i=1}^{N_\alpha} \sum_{j=1}^{N_\beta} \delta(r - |r_{ij}|) \tag{1.1}$$

10

where N denotes the coordination number, r is the radial distance, ρ is the number density of atoms, α and β are the atom types. Which in turn can be used to represent the total pair distribution function as Equation (1.2)

$$g(r) = \frac{N}{4\pi r^2 \rho N} \sum_{i=1}^{N} \sum_{j=1.J/i}^{N} \delta(r - |r_{ij}|) \tag{1.2}$$

in reciprocal space every partial pair distribution function has a partial structure factor which are related by a Fourier transform, Equation (1.3)

$$S_{\alpha\beta}(q) - 1 = \frac{4\pi\rho}{q} \int_0^\infty r[g_{\alpha\beta}(r) - 1] \sin(qr) dr \tag{1.3}$$

where q is the wave number in reciprocal space. Total structure factor is then defined as Equation (1.4)

$$S(q) = \sum_{\alpha} \sum_{\beta} \frac{c_\alpha c_\beta f_\alpha f_\beta}{(\sum_\alpha c_\alpha f_\alpha)^2} S_{\alpha\beta}(q) \tag{1.4}$$

where c_α and c_β are compositions and $f_{\alpha\ \beta}$ are the atomic scattering factors. Fourier transform of EXAFS data in real space and pair distribution function (PDF) data looks very similar. However their theory and experimentals measurements are quite different. EXAFS is measured at very distinct energy ranges and aimed at absorption edge of a certain element. So only atomic environmental data about that element is collected. This way chemically distinctive information can be collected but for the amorphous case after first neighbor shell data becomes uninterpretable. PDF on the other hand are not collected at a certain absorption edge energy, in fact quite excessive energies are used compared to absorption edges. So a total overall data from all constituents are collected and it is very difficult to separate these contributions as accurately as a EXAFS data. As an example to show the difference simulated EXAFS and PDF data of a gold nanoparticles system is given in Figure 1.9 [69].

1.5.2 Coordination Number

Definition and calculation of coordination number in crystalline and network glass systems is straightforward and well defined. However this is not the case for amorphous structures. There are four main definitions of coordination number: Cutoff distance method, Voronoi tessellation method, Delaunay method and closest nearest neighbor method. Easiest method amongst these is the cutoff distance method. Where

the first neighor shell distance is extracted from the position of the first peak in PDF data and this distance is drawn across a central atom. Number of atoms within distance is considered to be the coordination number. Second method is Voronoi tessellation where each of the central atoms which have voronoi shells that share a surface are considered to be neighbors. This method is independent of any parameters like distance. This measurement can be made with consideration of the atomic size (radical) or not (conventional). Delaunay triangulation is another alternative and the last one n-closest neighbor method uses predefined coordination number to extract which atoms are in the first neighbor shell. Figure 1.10 shows that coordination number is not unique and depends on method and definition [70].
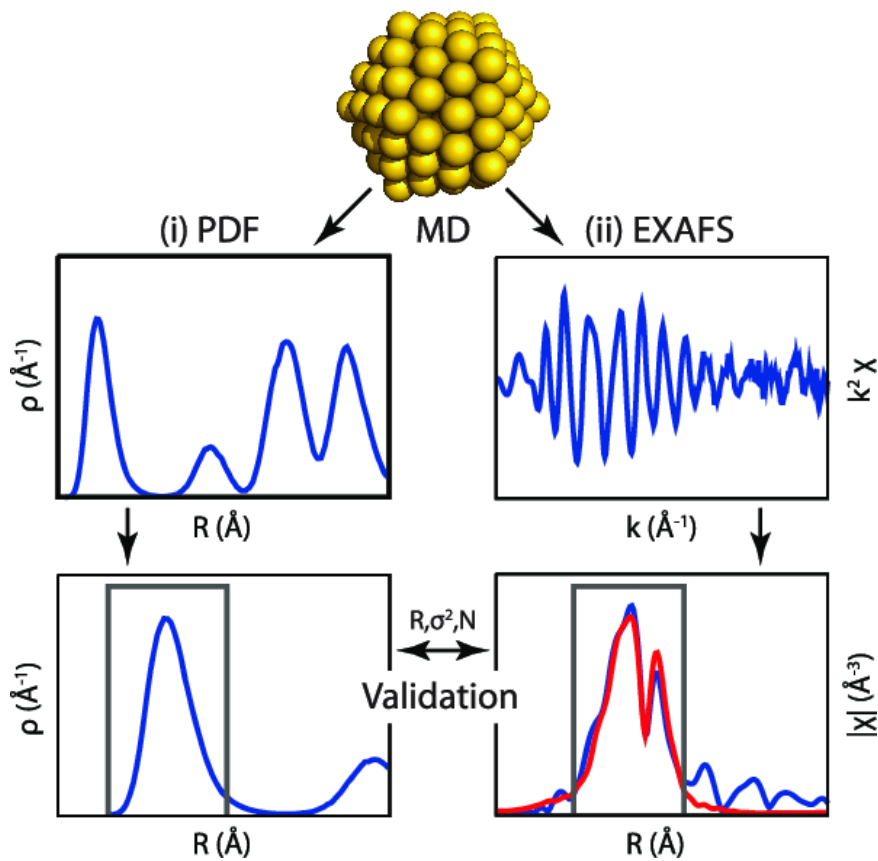
Figure 1.9: Simulated EXAFS and PDF data of Au nanoparticle system [69].
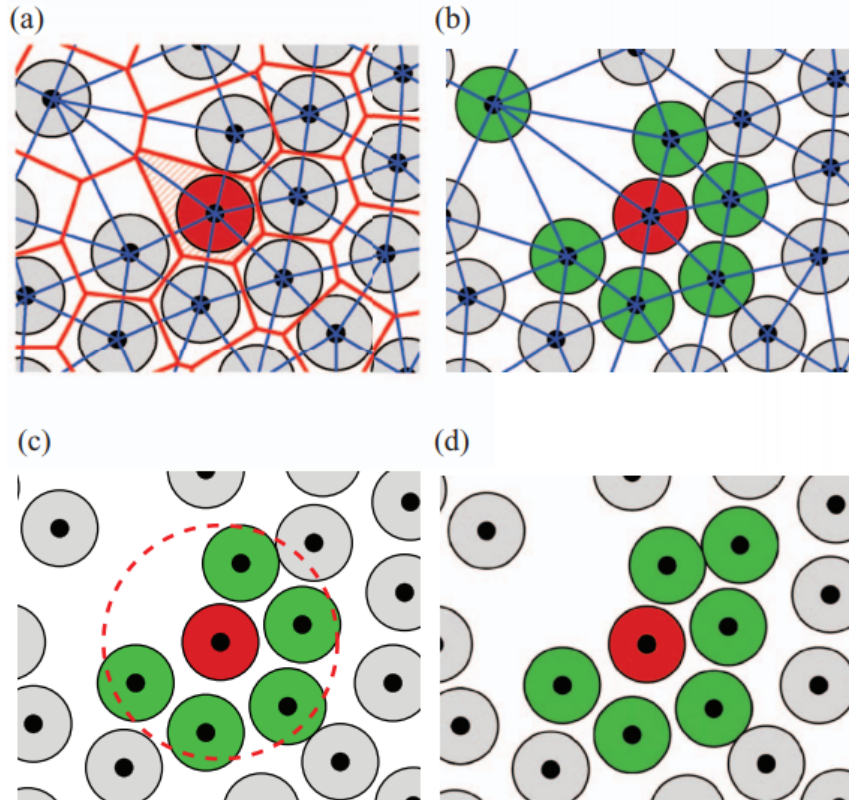
Figure 1.10: Coordination number definition and determination methods: a) Voronoi tessellation, b) Delaunay triangulation, c) cutoff radius and d) n-closest neighbor method [70].

1.5.3 Voronoi Tessellation

After its first discovered by Georgy Voronoy, Voronoi tessellation have been widely used in science, technology and arts. Voronoi diagram is a mathematical method that is used to divide 2 dimensional (2D) or 3 dimensional (3D) space into regions of central objects [71]. Its uses cover image processing, quadrature rules, clustering, cell division, territorial behavior of animals, non-euclidean metrics and so on [72]. In amorphous materials, it is used to determine coordination number without distance parameters and structural analysis. How it works is each atoms is considered as center separately, then a line is drawn from central atom to each neighbors, a plane is drawn from the mid section of these lines and in the end of each cell is created around each atom that represents the geometry of their neighbors [16,73] Figure 1.11. Created cell can be represented by its voronoi indices, which is a number vector $< i_3, i_4, i_5, i_6 >$

representing the number of triangles, quadrangels, pentragons and so on respectively. Most widely used open source library for Voronoi tesselation is the VORO++ which is designed specifically for cell based computations, 3D calculations and C++ architecture [74]. This software can be used for many walls, particle types, periodic or non periodic boundary conditions and radical/conventional methods Figure 1.12.
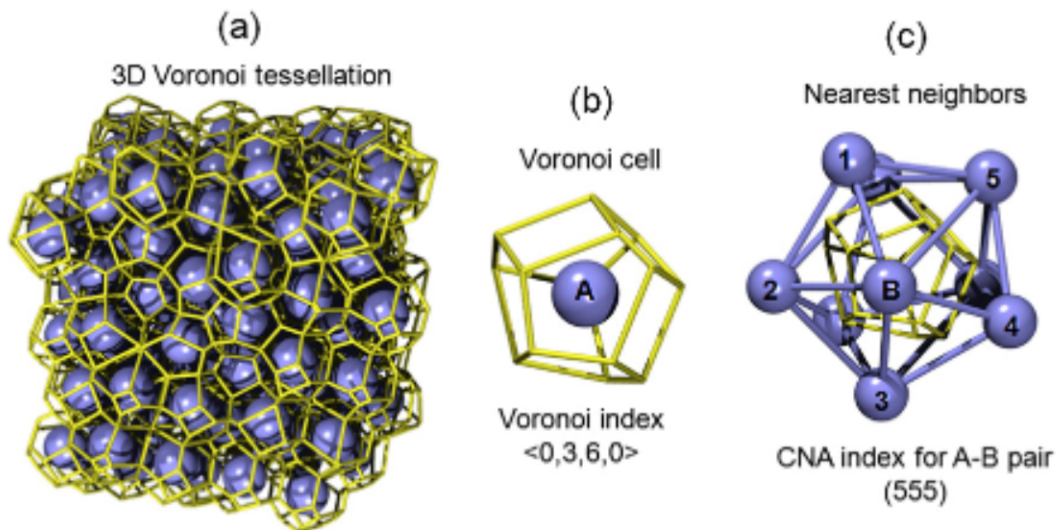
Figure 1.11: a) Voronoi tessellation, b) voronoi cell and c) the nearest neighbors [16].

Structural analysis of amorphous materials is much more complex then crystalline materials. However some of the most seen voronoi polyhedrals can be categorized under the structure of that they resemble for the sake of understanding. Fcc-like structure includes: <0,3,6,4>, <0,3,6,5>, <0,4,4,6>, <0,4,4,7>, Bcc like structure includes: <0,6,0,8> and Icosahedral-like structure includes: <0,0,12,0>, <0,1,10,X> and <0,2,8,X> where X=1,2,3,4 [16,75]. With increasing disclination these Voronoi polyhedrals can also be increased. Also in high atomic size mismatch systems, average coordination number may reach up to 16. These type of clusters can be collected under Frank-Kasper type structures.
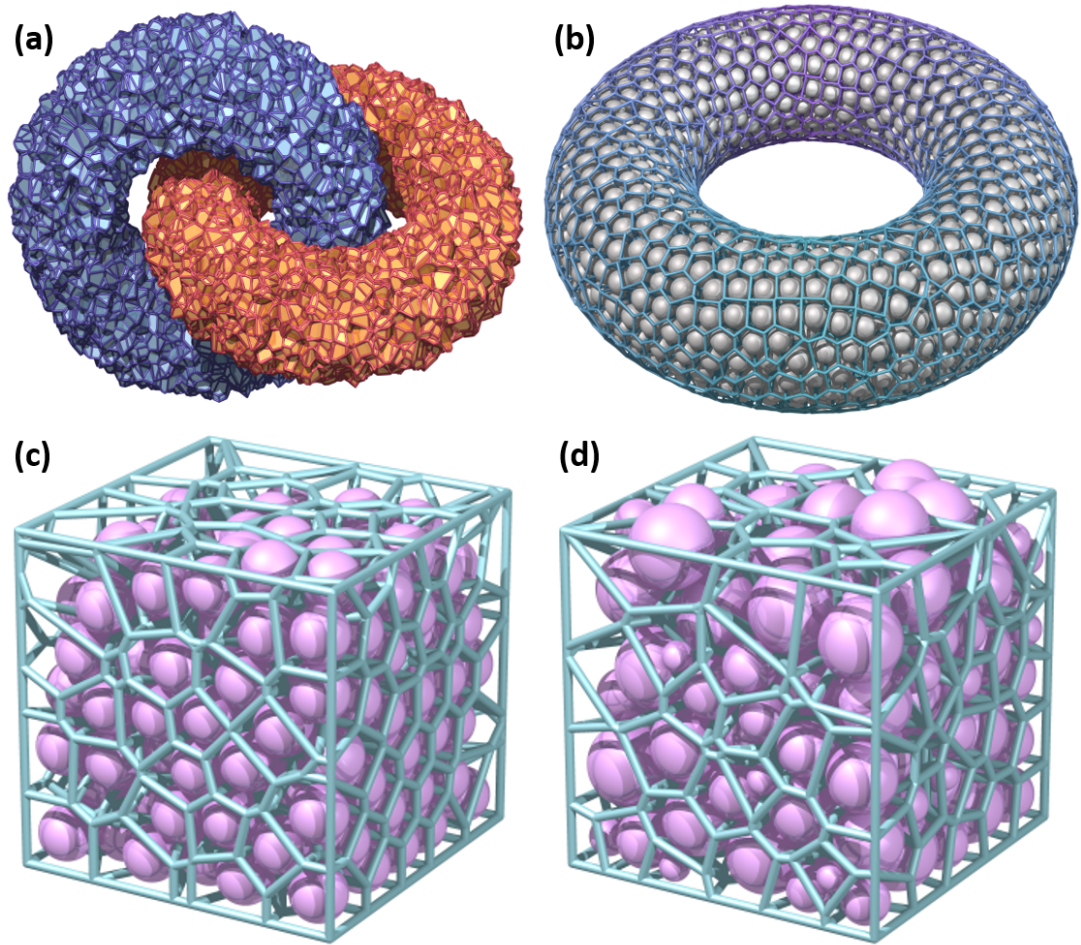
Figure 1.12: a) Loop case, b) Toroidal particle packing, c) conventional and d) radical voronoi tessellation [74].

1.6 Experimental Characterization Techniques

1.6.1 High Energy X-ray Diffraction

X-ray diffraction techniques have been used in materials research and specifically amorphous materials for a long time. From the earlier studies in 1930's [76] to the last decade there have been tremendous developments in X-ray diffraction analysis. Owing to developments in synchrotron technology todays measurements accuracy, data acquisition techniques, beam quality, modeling techniques and sophisticated experimental environments allows scientists to perform experiments that were thought impossible.

Synchrotron facilities are cyclic particle accelerators that are capable of producing extremely powerful rays. Synchrotrons consist of mainly four parts; linear accelerator (Linac), booster synchrotron, storage ring and beamlines Figure 1.13. Electrons are produces for the first time in Linac since synchrotrons reqire non-zero kinetic energy electrons to start the process. Produced electrons in Linac are accelerated enough to inject to booster synchrotron. Booster synchrotron is circular usually tens or hundreds of meters long accelerator where electrons can be accelerated up to billions of electron volts energy before being injected into storage ring. Storage ring is where electrons travel close to speed of light. The structure contains different types of magnets to produce X-rays. Finally, beamlines are experimental halls where X-ray beams are directed from the storage ring. Each beamline in a synchrotron have a distinct energy range and purpose therefore designed for that purpose. Total scattering experiment
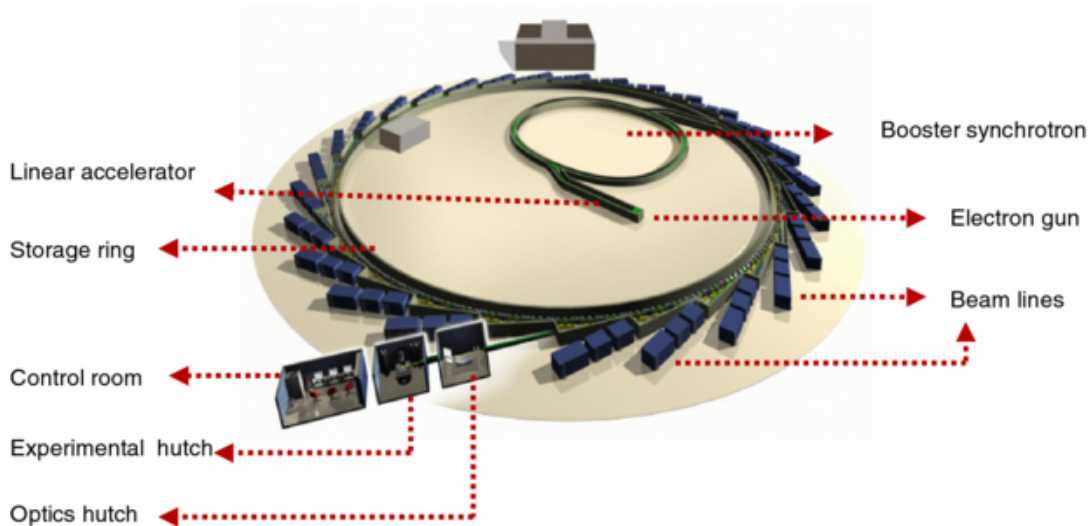
Figure 1.13: Schematic outline of Diamond Light Source [Image retrieved from [77]]

data from synchrotron light source, although having excellent resolution also contains various noise signals. These noise signals must be excluded and corrections must be made in order to obtain total structure factor Egami [67, 78]. Total structure factor is expressed by Equation (1.5)

$$S(Q) = \frac{I_C(Q) - \sum_{i=1}^{n} a_i \left| f_i(Q) \right|^2}{\left| \sum_{i=1}^{n} a_i f_i(Q) \right|^2} \tag{1.5}$$

where $I_C(Q)$ is coherently scattered X-ray intensity and $f_i(Q)$ is atomic scattering factor.

1.6.2   X-ray Absorption Fine Structure

X-ray absorption spectroscopy refers to how X-rays are absorbed as a function of energy. Which is governed by $E = h.w$ where as absorption as a function of distance is expressed by Equation (1.6) and Figure 1.14

$$I = I_0 e^{-\mu x} \tag{1.6}$$
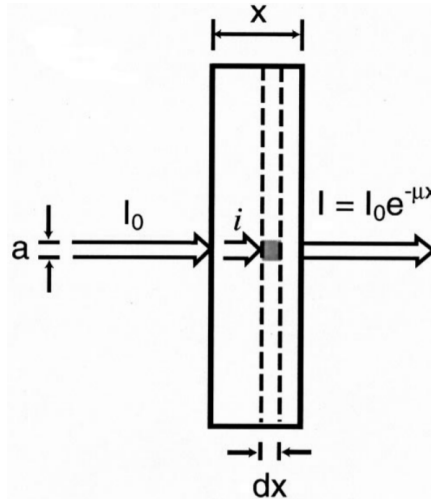
Figure 1.14: Schematic view of X-ray absorption

XAFS on the other hand refers to structural oscillations on the absorption edge of the target material. XAFS spectroscopy is a unique tool for investigation of local structure around selected elements. Although the XAS and XAFS have similar physical basis they differ on approximations, techniques, terminology and approaches. XAFS spectrum forms X-ray photoelectric effect where a sample is bombarded with X-rays within a certain energy range that covers the absorption edges of target element. When this X-ray photon liberates an electron from the target element, photo electronic wave scattering occurs it reacts and forms interference with the incoming and outgoing photo-electronic waves. As an example Figure 1.15 is given where XAFS spectrum of iron-sulfur-lithium nanocomposite can be seen [68, 79–81]. Carefull investigation of XAFS spectrum can reveal information about the average bond distances of the neighboring shells, coordination numbers, absorber oxidation states, coordination geometry, structural disorder and thermal motions. It can also be used

as a finger print method where certain percentages of products in a reaction can be measured simultaneously.
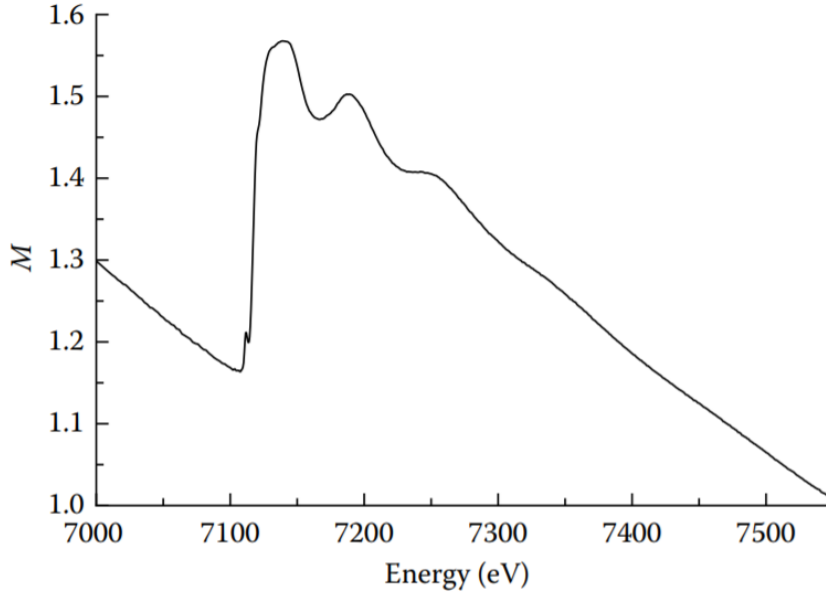
Figure 1.15: XAFS spectrum of iron-sulfur-lithium nanocomposite [79].

XAFS spectrum consists of two main regions; X-ray absorption near edge structure (XANES) and EXAFS region where peaks shoulders, other features near or on the edge and gradual oscillations above the edge are seen Figure 1.15. In this study EXAFS analysis is used since the structure around target elements is under investigation.

$$\chi(k) = S_0^2 \sum_i N_i \frac{f_i(k)}{kR_i^2} e^{-\frac{2R_i}{\lambda(k)}} e^{-2k^2\sigma_i^2} \sin(2kR_i + \delta_i(k)) \qquad (1.7)$$

EXAFS signal is governed the EXAFS equation, Equation (1.7) where k is the wave number, S_0^2 is the amplitude reduction factor, N is the degeneracy and coordination number, $f(k)$ is the elastic scattering proportionality constant (Scattering amplitude) together with kR_i^2 they represent elastic scattering probability, $\sin(2kR_i + \delta_i(k))$ term accounts for phase shift, D is the distance from absorber atom to scattering atom (half length of the scattering path), σ_i^2 is the variance in the R_i due to disorder (Debye-Waller Factor) and $\lambda(k)$ is the mean free path of the photoelectron. It should be kept in mind that there are different versions of EXAFS equations which are focusing on different aspects using different conventions, equation given above is the one that is

18

used by EXAFS society.

There are two modes of measurement in XAFS; transmission and fluorescence both having certain advantages and disadvantages depending on sample and environment. Transmission mode while requiring high concentration and homogeneous samples without pinholes etc. requires properly aligned beams. Also when the material under investigation is in powder form there are certain grain size restrictions depending on the absorption length. Sample thickness is also another important deciding factor for fluorescence and transmission modes. Usually for metal and oxide bulk materials thickness lower limit is from five to tens of microns. Fluorescence method is somewhat more complicated but gives better results when sample is too thick or have higher concentrations. Main consideration when making a good fluorescence measurement covers energy resolution, solid angle and self absorption.

1.7 Modeling and Simulation Techniques

1.7.1 Reverse Monte Carlo

Reverse Monte Carlo is a simulation technique that is capable of building 3D structural models derived directly from the experimental data without assuming any prior models. RMC method can be shortly explained as:

(i) Initially a configuration of atoms is fed to the system. This could be a random array of points, a lattice or coordinates generated from other simulation methods. Only restriction here is that it must be a cubic simulation box.

(ii) Number density and cutoff distances for atomic pairs must be provided for a sound and accurate simulation.

(iii) Usually periodic boundary conditions are applied and simulation box is multiplied by itself to create radial distribution function. However if simulation box is big enough non-periodic boundary conditions can be applied.

(iv) Simulated experimental data sets are then calculated for the initial atomic configuration.

(v) A single atom is moved and a new atomic configuration is created. New simulated experimental data sets are again calculated.

(vi) The new data and old data are then compared with χ^2 test.

(vii) If the new configuration is closer to experimental data restrictions the move is accepted. If not the move accepted or rejected with a probability determined by user.

(viii) The move is accepted then new configuration becomes starting configuration if not old configuration is retained and move is discarded.

(ix) Given metropolis loop is repeated until χ^2 decreases and oscillates around an acceptable value [82].

There are various experimental and computational restrictions that can be applied to increase the accuracy of the simulation. Main experimental data restrictions are X-ray diffraction, neutron diffraction, XAFS, electron diffraction, raman spectroscopy, nuclear magnetic resonance spectroscopy and transmission electron microscopy data but technically any experimental data set that can be expressed as an equation of atomic positions can be used. Computational restrictions are mainly, atomic potentials, coordination number constraints, fixed neighbor constraints, geometric constraints, second neighbor constraints, local invariance, periodic on non-periodic boundaries, atomic vibrational constraints and so on [83]. RMC method is commonly used for particularly amorphous systems but it can also be used for polymers, crystals and magnetic materials. Figure 1.16 shows how well RMC can create atomic models that can represent the given experimental data sets.

Representativeness and uniqueness are the two most important requirements when modeling a amorphous structure. All computer simulation methods have their advantages and disadvantages. Therefore using as many experimental data and as many different simulation methods is key to extract the true structural features. For example metallic glass systems require quite high cooling rates and this can be a problem for *ab-initio* molecular dynamics simulations because system requires longer time periods to reorganize its temperature/density which is not computationally feasible. However relaxation process with molecular dynamics is highly beneficial for this
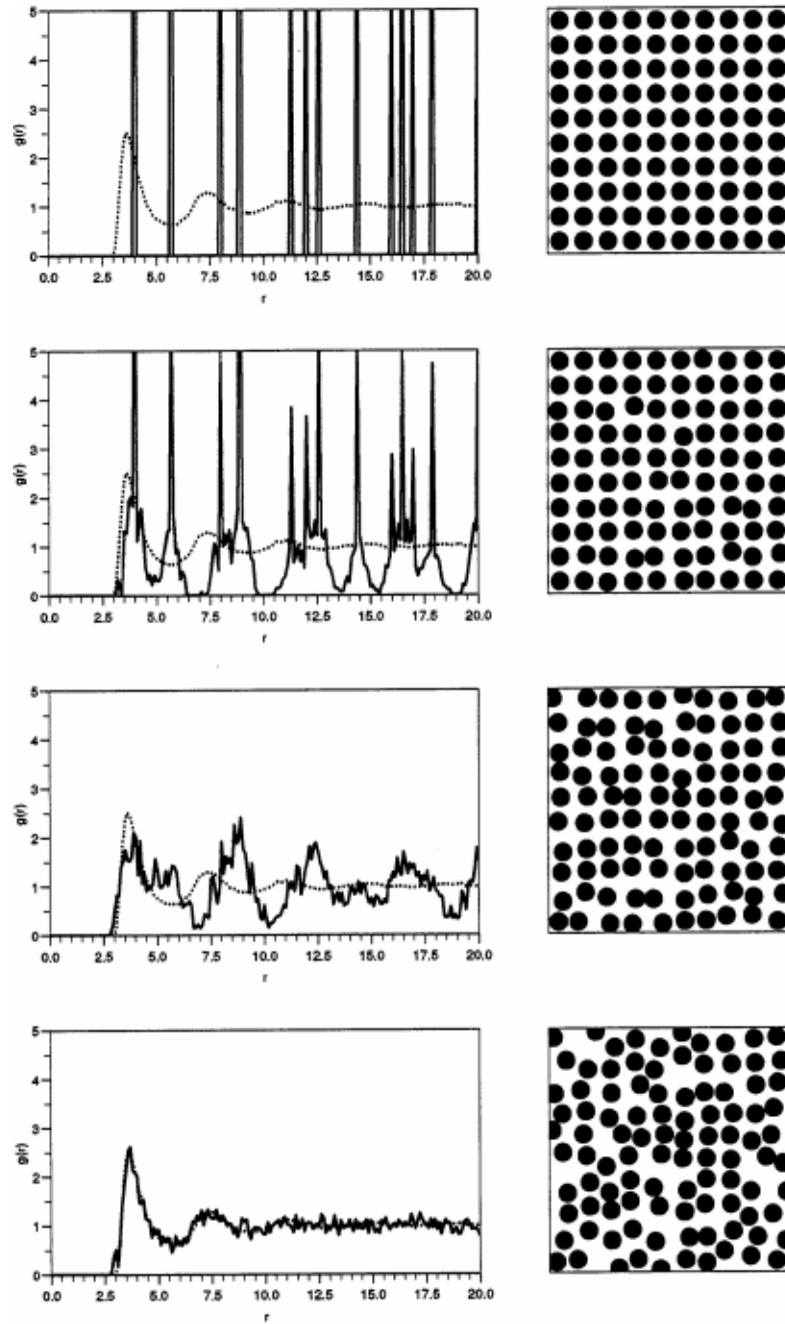
Figure 1.16: Experimental data sets and corresponding 2D RMC models created by 2500 accepted moves with Lennard-Jones potentials used as constraints on the system.

kind of structures. Another important point is that in order to investigate order in medium range simulation box must be sufficiently big. MD simulation boxes are rather smaller in this aspect so they require usually multiple simulations to reduce

noise levels in data. RMC method on the other hand have much higher simulation box that can easily represent medium range order without computational conflicts. Its reliability is independent of the cooling rate and it does not require a prior model to run the simulations. Because of these reasons it is widely used to create atomic models of amorphous structures. However it is not unique, as in consecutive simulations may result in different outcomes even though experimental data fits are on the same level of goodness. It is proven that RMC method seeks out the highest degree of entropy so results are more disordered than target structures. Because of these reasons in order to perform a reliable RMC simulation, multiple experimental data restrictions must be used and results must be double checked with an independent auxiliary method [84].

1.7.2 EXAFS modeling

After the data collection is complete EXAFS analysis consists of two parts; data reduction and data modeling. There are various software packages used for XAFS analysis, VIPER and DEMETER being the most widely used ones. Most of these softwares have the same capabilities with different user interfaces but for this study DEMETER software package is used due to its user base being more active. DEMETER package contains 3 softwares: HEPHAESTUS which has a periodic table with focused information about absorption, ATHENA which is used for XAS data processing and ARTEMIS used for EXAFS analysis and modeling accompanied by FEFF and IFEFFIT .

Data reduction part of XAFS analysis may seem straight forward but it is the most crucial part. Since any mistakes here effects the EXAFS modeling part and result in unreliable fits. Main steps of XAFS data reduction are listed below. Data reduction steps in DEMETER:

(i) Data is uploaded to ATHENA software, data type is chosen as $\mu(E)$ with energy column vs. I_0/I_1 data drawn. All of the data collection channels must be activated so that average is taken and noise level is reduced. (It is important that Natural log button is activated for Transmission data, Fluorescence data is

direct fraction.)

(ii) Reference channel must be activated. (Reference data is used for data alignment if necessary.)

(iii) Rebinning of the data set is used only if data is collected at quick scan mode in synchrotron. This improves the statistical value of the data is EXAFS region.

(iv) Normalization of data: Choosing pre-edge and normalization range for subtraction

(v) Background removal from data: $rbkg$ parameter is chosen to remove background by taking frequency cut-off in to account [85].

(vi) K-weight parameter is used for data plotting and Fourier transforms. This value must be chosen in accordance with which part of the XAFS spectrum is most important and must be amplified while reducing noise levels.

(vii) Threshold energy E_0 must be chosen by either derivative method, or by rising part of the XANES region method. (This parameter must be changed if E_0 is unrealistic after EXAFS fitting.)

(viii) Forward Fourier transform k-range must be chosen by maximizing the amount of data but not so much that noise is considered to be the data in long k-range.

(ix) Backward Fourier Transform R-range must be chosen. (if data under consideration is amorphous choosing a range that only covers the main amorphous peak is enough.)

(x) Aligning of the data taken at consecutive measurements must be done by aligning the reference data

(xi) Deglitching, truncation, smoothing convolution and/or deconvolution of the data can be done depending on the noise levels and energy glitches in the data.

(xii) Finally consecutive measurements are merged and data is ready for EXAFS modeling.

EXAFS modeling gives accurate and crucial information about the neigbouring atoms, bonds lengths and chemistry [68, 79]. EXAFS modeling is a long and complicated

subject with so strict rules and every substance under investigation can have its own solutions and tricks. In this part specific solution to analyze $Al_{90}Tb_{10}$ system will be given which can be applied to many amorphous systems. EXAFS modeling works best when there are some priori knowledge about the system under investigation. Process starts with finding a model system that is similar and running a FEFF simulation on that simulation. The most tricky part of an EXAFS modeling on amorphous systems is finding the atomic model. Since amorphous systems are not recorded standards as crystals. However starting with a crystal system with similar atomic environments and bond lengths is usually enough to begin with. Afterwards some parameters are derived from that model and some are floated in experimental data until a fit that is "defendable" is obtained. The term "defendable" is used since there are no absolute right or end to EXAFS modeling. Even after finding the right model and doing the right simulations one can improve the fits insignificantly by just changing certain parameters. Parameters of phase shift $\delta_i(k)$, mean free path $\lambda(k)$, degeneracy N_i and scattering amplitude $f_i(k)$ are obtained from the FEFF calculation of the model atomic system. The remaining parameters of amplitude reduction S_0^2, Debye-Waller factor σ_i^2 and half length of scattering path (atomc distance of neighbor atom) R_i are fitted to the experimental data. Coordination number calculation introduces a change in to this approach. In order to calculate the Coordination number and amplitude reduction factor was so far used as a single parameter and calculated together must be separated as fixing degeneracy term to 1 and introducing coordination number as a separate term. This also requires to fix the amplitude reduction factor which can change from even measurement to measurement in synchrotron. However this term is not affected from the atomic environment so the best course of action is to use a reference material as the same element of the measurement. Calculating the amplitude reduction for a pure element is a easy task and using that factor in the EXAFS modeling decreases the unknown parameters by one and allows for the calculation of coordination number [86]. An example of the CN calculation is given in chapter 2. EXAFS modeling continues with fitting the parameters to peaks in the data one by one until mathematically and physically meaningful results are obtained.

1.8 Thesis Organization

Marginal metallic glasses have intriguing structural attributes and superior properties both in fully amorphous and partially crystallized states. Aim of this study is to have a better understanding of structural arrangements in these alloys, how it is inherited, how it affects the devitrification behavior and finally how do they perform mechanically. To that end a series of studies were conducted.

First chapter includes a brief introduction from general to specific as amorphous materials, metallic glasses, Al-based marginal metallic glasses. Basic information related to thermodynamics, kinetics and structural analysis methods necessary to understand the study. Followed by a short descriptions of experimental and computational methods used throughout the study. Second chapter is specific to structural analysis of $Al_{90}Tb_{10}$ metallic glass, effect of amorphous precursors used in two different production routes, how it results in different devitrification hierarchy and final products. HEXRD, XAFS and RMC studies concluded that the melt-spun ribbon solidifying from liquid state have a higher degree of order than magnetron sputtered film solidifying directly from gaseous state raising the question of "Is liquid state not as homogeneous as it is previously considered?". Finally this dissimilarity in structural order results in differences in devitrification behavior. Third chapter is devoted to mechanical testing where FIB milled micropillars were tested under compression. Stress vs. strain graph and fracture surfaces have shown that embedding crystals in matrix increases strength without causing brittleness. Where as introducing intermetallic compound increases fracture stress while decreasing toughness. Final chapter includes conclusions, ongoing studies and future recommendations.

CHAPTER 2

THE ANOMALOUS NUCLEATION IN AL-TB METALLIC GLASSES

2.1 Introduction

Attributed primarily to its stringent properties, metallic glasses have been considered as promising materials for engineering applications [16, 87–93]. On the other hand, full application of metallic glasses is limited because of their near-zero ductility [24, 93, 94]. Due to the formation of highly localized strain during deformation, metallic glasses fail catastrophically after yielding. Metallic glass/nanocrystal composites, on the other hand, have shown improved ductility over the monolithic glass. Such composite materials can be either prepared through direct solidification [95–97] from the melt or partial crystallization of metallic glasses by heat treatment or deformation [28, 30] Among the metallic glass/nanocrystal composites, Al-RE alloys have remarkable significance. Partial devitrification of the Al-RE marginal metallic glasses results in the anomalous number of nanocrystals, on the order of $10^{21} \, \mathrm{m}^{-3}$ to $10^{24} \, \mathrm{m}^{-3}$, embedded in the amorphous matrix [42, 98–100]. Despite the volume of the research, an exact explanation for the mechanism underlying the formation of highly populated nanocrystals is still missing [22, 99, 101] So far, attempts to explain this high nucleation density speculate around several models such as "quenched-in nuclei" [100, 102], "phase separation in the amorphous state" [103–105], and "heterogeneous nucleation" [106]. "Quenched-in nuclei model" is stating that some small fractions of crystallites form initially during cooling but their development is prevented by rapidly increasing viscosity with continued cooling near glass transition temperature (T_g). Upon reheating a sample with preexisting crystallites, rapid crystallization ensues at T_g and these preexisting crystallites grow to nanocrystals. "Phase separation in the amorphous state" relies on phase separation similar to spinodal de-

composition resulting in heterogeneous nucleation at the phase boundaries. According to this approach a time dependent homogeneous nucleation occurs as a result of the formation of Al rich and Al depleted zones with length of 74 to 126 nm [105]. The other hypothesis to describe the observed high nucleation densities of nanocrystals is the possibility of an extremely large number of heterogeneous nucleation occurring on either impurity site such as nano-scale oxides [107] or clusters of inhomogeneously distributed atoms [106]. This hypothesis is only observed for a few multicomponent amorphous systems and it is still under question since the density of impurities are usually orders of magnitudes lower than the number of nanocrystals formed during devitrification. Consequently, there is still no agreement on the mechanism of highly populated nanocrystal formation in marginally metallic glass forming alloys.

We believe that fcc like medium range order MRO structures that are inherited from the parental liquid state plays a crucial role in abnormal nanocrystallization of Al-RE (and possibly in other Al-RE-TM) metallic glass alloys [108]. In order to further prove that MRO might be originated in the liquid form, we have produced amorphous Al-RE with exactly same composition but using different processing techniques. A first set of $Al_{90}Tb_{10}$ was produced using melt-spinning and the second set with exactly the same composition was produced using DC magnetron sputtering [109]. The phase selection hierarchy of these glassy alloys produced by two different techniques was investigated. Although the fcc-Al nanocrystals were observed as the primary devitrification product in both specimens, the morphology, the average size, and the nucleation density are substantially different. Further investigation also showed that ribbons devitrifies with a metastable hexagonal phase and transforms into metastable cubic phase. On the other hand, the sputtered thin-film suppressed the hexagonal phase and directly changes into cubic phase directly upon crystallization. The difference between the crystallization of as-sputtered and as-spun of $Al_{90}Tb_{10}$ was also detected in thermal analysis results. It was claimed that these differences may be associated with the degree of topological and chemical order within the amorphous precursors. According to this hypothesis, chemical separation up to some degree has already established in the ribbons that were quenched from the liquid state. We believe that this separation was inherited from the liquid state in the melt-spun ribbons [108, 109]. On the other hand, a full description of amorphous structures in

28

melt-spun ribbon and sputtered thin-film via advanced characterization techniques is still missing.

In this study HEXRD and XAFS experimental methods coupled with Reverse Monte Carlo simulations and Voronoi tessellation are used to examine the atomic structures formed in melt-spun ribbon and magnetron sputtered film $Al_{90}Tb_{10}$ alloys. Short-range order (SRO) and MRO in resulting structures are revealed by first neighbor shell and cluster analysis, respectively. TEM analyses were conducted to reveal the fundamental structural difference in ribbons and thin-films in early crystallization periods.

2.2 Experimental

Ingots of $Al_{90}Tb_{10}$ were produced by arc-melting from highly pure Al (99.99 wt. %) and Tb (99.9 wt. %) elements in argon atmosphere and re-melted three times for chemical homogeneity. Amorphous melt-spun ribbons were produced by a single copper block jet melt-spinner with $25\,\mu m$ thickness and $12\,mm$ width by quenching from $1423\,K$ at a tangential wheel speed of $30\,m\,s^{-1}$. Amorphous thin-films were produced by direct current magnetron sputtering on a liquid nitrogen cooled Si wafer. Both samples produced in AMES laboratory.

X-ray diffraction experiments were performed at BL04-MSPD beamline of ALBA synchrotron facility in transmission mode using a wavelength of $0.4136\,\text{Å}$ with double Si monochromator. The diffraction data were collected in the Q-range ($Q = 4\pi \sin{(\theta(\,/\lambda)}$ where θ is the Bragg's angle and λ is the wavelength of X-ray radiation) of 0.83–7.5 Å^{-1} using a Mythen array detector system. Intensity versus Bragg angle data were first corrected for background, polarization, absorption and multiple Compton scattering then converted in to total X-ray structure factor using PDFgetX3 software [78].

XAFS measurements were performed at CLAESS beamline of ALBA using a double-crystal Si (1 1 1) monochromator at Terbium L3 edge. Ionization chambers are filled with N_2, He and Kr gasses. Silicon-drift and CdTe single channel fluorescence detectors were used to collect data in transmission and fluorescence modes, for melt-spun ribbons and magnetron sputtered films, respectively. Co is used as energy reference

and simultaneously measured with the samples. 3 different scans performed and data obtained simultaneously from different channels were averaged to form XAFS spectrum. DEMETER software was used for data processing and model fitting [110]. A crystal structure of Al-Tb with similar atomic environments to its amorphous counterpart is used for EXAFS modelling.

RMC simulations were initiated using `RMC_POT` package with `RMC_Multi` implementation with a 30,000 atoms cubic simulation box of $83\,\text{Å}$ edge length with periodic boundary conditions. RMC was constrained by density, cut-off distances obtained from ab-initio molecular dynamics (AIMD) and XRD, EXAFS experimental data. Calculated coherent structure factor $S(Q)$ from X-ray diffraction data and calculated $\chi(k)$ data from EXAFS were fitted to their experimental values. Due to its nature, $\chi(k)$ data contain larger noise signals which can be detrimental to the RMC fitting. Therefore while XRD data is fitted as is, EXAFS data is imported in k space then filtered via Savitsky-Golay method to avoid degrading peaks while reducing noise levels [79, 111]. The difference between experimental and calculated values for $S(Q)$ and $\chi(k)$ are calculated and minimized according to Equation (2.1)

$$\chi_k^2 = \frac{\sum_k (S_i^C(Q_k) - S_i^E(Q_k))^2}{\sigma_i^2} \tag{2.1}$$

and

$$\chi_i^2 = \frac{\sum_{J=1}^{NPoints} (\sigma_i E_i^E(k_j) + b_i - E_i^C(k_j))^2}{\sigma_i^2} \tag{2.2}$$

respectively where S_i^C, S_i^E, E_i^E, E_i^C are computed and experimental structure factors and EXAFS data respectively. Whereas σ contains the weight of data set used in the fitting procedure [112]. Structural arrangements in the system analyzed by means of Voronoi tessellation with VORO++ software [74]. Voronoi tessellation is a method to divide 3D space into Voronoi cells by creating shared planes with center atom to neighbor atoms. Voronoi cells are formed with these planes which are denoted by indices $n3, n4, n5, n6, n7, n8$ where ni is the number of edges each Voronoi surface has [16, 113]. Radical Voronoi tessellation with periodic boundary conditions on a cubic simulation box is used due to the large atomic size difference between Al and Tb atoms.

Specimens for TEM analyses were prepared using electropolishing with a solution of 25 vol.% nitric acid and 75 vol.% methanol at $241\,\mathrm{K}$.

Differential scanning calorimetry (DSC) measurements were performed at 4 different heating rates as 10, 20, 30, and $40\,\mathrm{K\,min^{-1}}$ from room temperature to $773\,\mathrm{K}$ under N_2 atmosphere. DSC traces were then used in Kissinger and Ozawa-Matusita analyses to calculate the activation energies of first crystallization event for ribbon and thin-film samples. Kissinger relationship for non-isothermal reactions is controlled by Equation (2.3) [114];

$$\ln(\phi/T_p^2) = \mathrm{const.}(-E_c/RT_p) \tag{2.3}$$

where ϕ is the heating rate, T_p is the peak temperature, E_c is the activation energy and R is the gas constant. Whereas in Ozawa-Matusita method degree of reaction is assumed to be constant and independent from heating rate as in Equation (2.4) [115];

$$ln(\phi) = \mathrm{const.}(-1.052E_c/RT_p) \tag{2.4}$$

Activation energies of the first fcc Al crystallization for ribbons and thin-films were then obtained from the slopes of $\ln\left(\phi/T_p^2\right)$ vs $1/T_p$ and $\ln\left(\phi\right)$ vs $1/T_p$ plots.

2.3 Results and Discussion

In order to confirm the amorphous nature of the $Al_{90}Tb_{10}$ melt-spun ribbons and magnetron sputtered thin-films synchrotron based XRD experiments were conducted. Figure 2.1 shows the $S(Q)-Q$ data with amorphous humps and accompanied pre and side peaks that are characteristics of Al-RE marginal metallic glasses. The pre and side peak formations were previously studied for Al-RE marginal metallic glasses [16, 116]. The existence of pre-peak and side-peak reflections located at approximately 1.3 and 3.4 $\mathrm{\mathring{A}}^{-1}$ are indications of a pseudo-order in amorphous structure [44, 109].
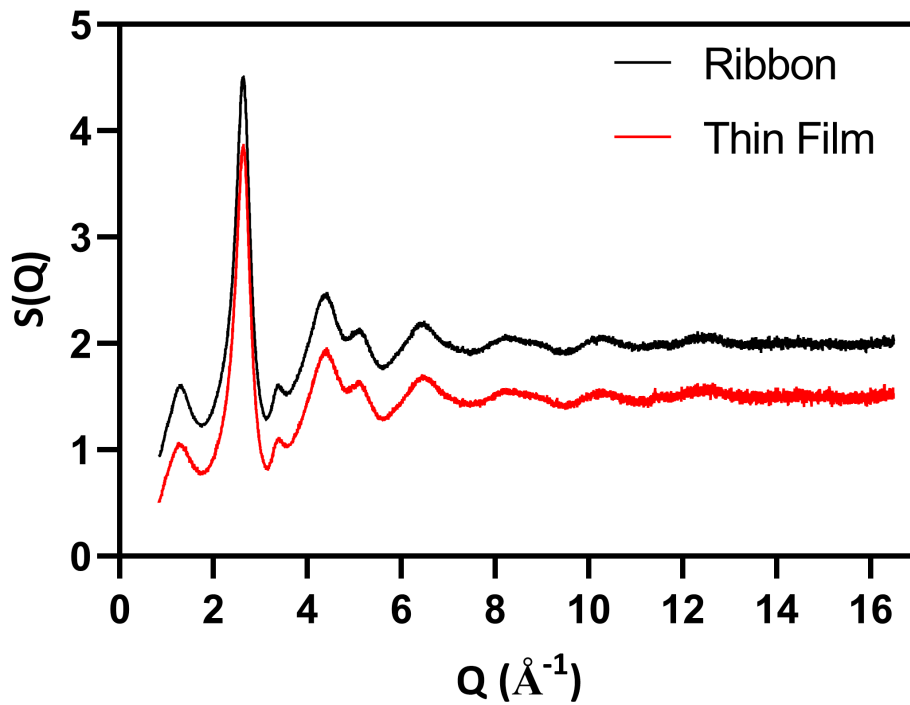
Figure 2.1: Total X-ray structure factors of melt-spun ribbon and magnetron sputtered thin-film.

RMC simulation is widely used for the structural analysis of the amorphous materials due to its practical ability to derive three-dimensional configuration of atoms directly from experimental data without assuming any prior candidate models [117]. However, using RMC with only $S(Q) - Q$ can be misleading since $S(Q) - Q$ is a one-dimensional data without absolute ability to discriminate among models that can result in the same XRD pattern. At that point using other experimental constraints which are sensitive to chemistry and local atomic structure such as EXAFS is crucial to create models closest to true atomic structure. In that sense, we have coupled our $S(Q) - Q$ data with Tb L_3 edge EXAFS spectra and cut-off distances to obtain the most representative 3D atomic configuration of amorphous structure using RMC. Figure 2.2 shows the experimental HEXRD and EXAFS data with corresponding RMC fits. For the ribbon XRD data are almost in perfect agreement with the RMC fit. EXAFS data, on the other hand, have reasonably good fit, due to the fact that EXAFS has restricted data points when compared to $S(Q)$ due to its derivation. Beyond that,

fit is almost perfect in the range of 6 to 10 Å^{-1} and in earlier k space it is perfectly in phase with the data with small amplitude differences. A similar situation is also valid for the thin-film data. After an approximate 108 iterations, a cubic simulation box with 30000 atoms and edge length of 8.30 nm is obtained as shown in Figure 2.3 (a). RMC simulations were repeated 12 times with 3 different processors. Besides smaller statistical differences all of the simulations give similar results both numerically and comparatively between ribbon and thin-film samples.
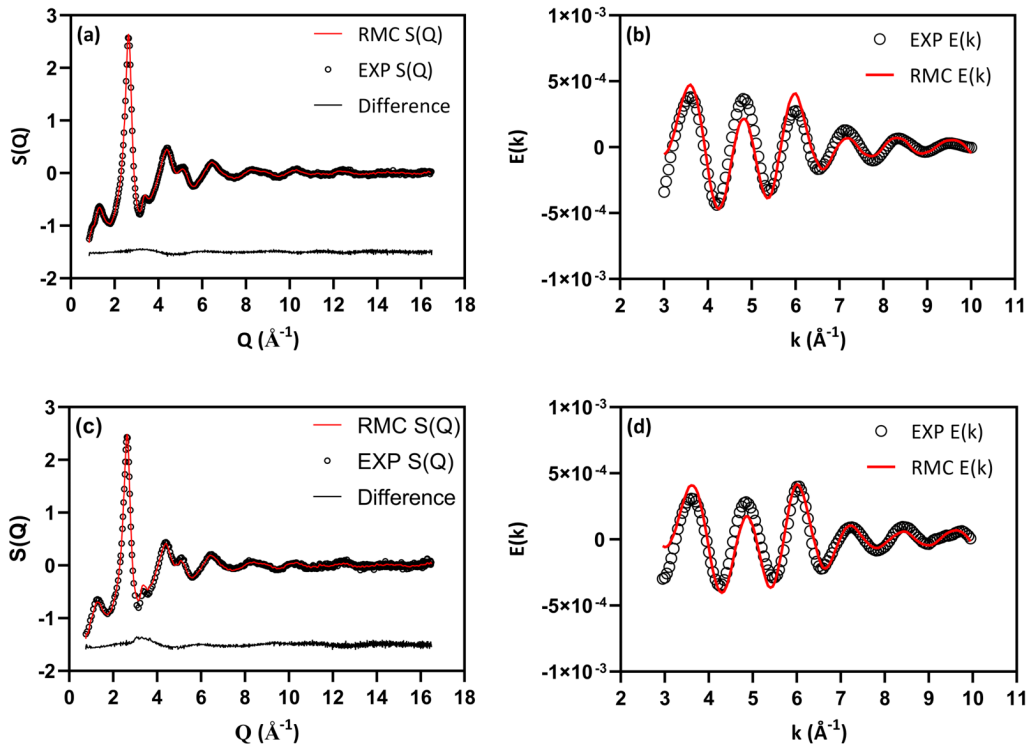
Figure 2.2: (a), (c) Total X-ray structure factors and (b), (d) EXAFS experimental data with their corresponding RMC fits for melt-spun ribbon and magnetron sputtered film, respectively.

In order to characterize the local atomic environment in RMC simulated configurations Voronoi tessellation method [74, 113] is used. Voronoi polyhedra (VP) are analyzed under Al centered and Tb centered subclasses. 15 most populated VPs for melt-spun ribbons and magnetron sputtered samples are given in Figure 2.4. Most populated Al centered clusters are <0,3,6,4> and <0,2,8,4> types for both ribbon and sputtered samples. For Tb centered clusters, VPs with higher coordination number
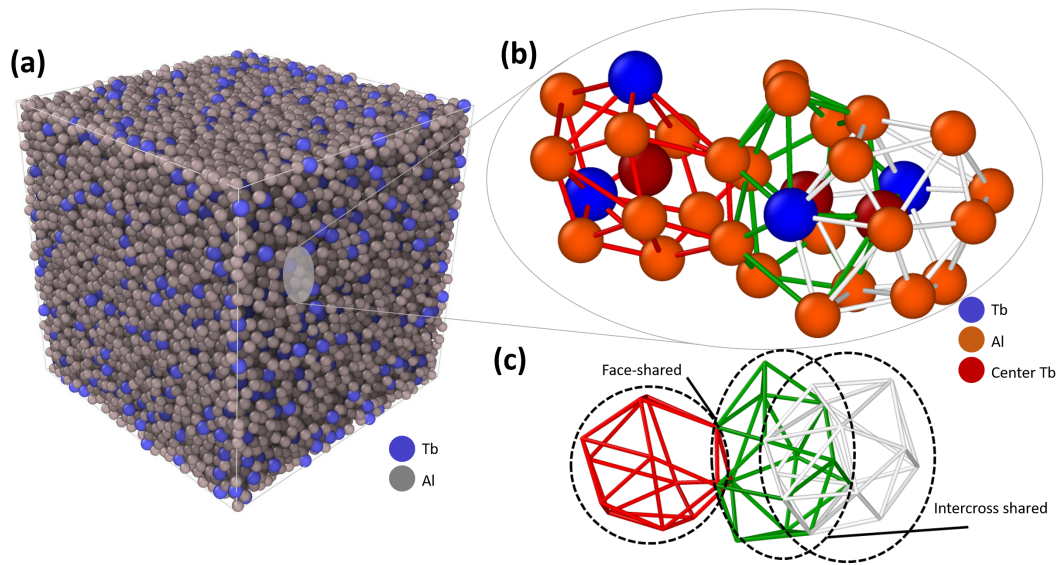
Figure 2.3: (a) RMC simulation box after fitting, (b) close up view of triple <0,3,6,4> Voronoi cell interacting with each other and (c) Voronoi cells with face and intercross sharing.

(CN) i.e. <0,2,8,5>, <0,2,8,6>, <0,1,10,4> and <0,1,10,5> are found to dominate the configuration. Another interesting point is that for Al centered cluster most of the VPs in ribbon have a higher population than the ones in sputtered samples. Although the difference seems to be small it is always present in most of the Voronoi cells and in all other consecutive simulations. So, it is safe to say that short range structural order is more pronounced in melt-spun ribbons. This difference is believed to be originated due to different processing history of amorphous precursors as melt-spun ribbons solidify from liquid state and thin-films form from gaseous phase. Ribbon and sputtered samples have similar CN values, as seen in Figure 2.4. On average Tb centered clusters has 16 neighboring atoms and Al centered clusters have 14. In order to have a full understanding of short-range order throughout the simulation cell VPs are categorized in accordance with the main structures they resemble as seen in Figure 2.4. Al centered VPs are categorized as fcc-like: <0,3,6,4>, <0,3,6,5>,0,4,4,6>, <0,4,4,7>, icosahedral like (ICO): <0,2,8,X>, <0,1,10,X>, <0,0,12,0>, where X= 1,2,3,4 and 5 [16]; Tb centered VPs are analyzed under same categories with the addition of high coordination number Frank-Kasper Z15: <0,0,12,3> (with increasing disclination density <0,1,10,4>, <0,2,8,5>, <0,3,6,6>) and Z16: <0,0,12,4> (with increasing

34

disclination density <0,1,10,5>, <0,2,8,6>, <0,3,6,7>) type cells [16]. Al centered VPs are mostly dominated by ICO-like and fcc-like clusters where ribbons having higher amounts indicating more ordered structure than sputter. Tb centered VPs have a more dominating structure than Al centered VPs as Frank-Kasper Z15, Z16 types. Again, in these clusters, ribbons have higher percentage than sputtered samples in all three categories. Supporting the idea that the amorphous precursor type in the samples having the same composition resulting in order-wise different structures. RMC can lead to energetically unfavorable models due to lack of chemical interaction [84, 118]. In order to overcome this uncertainty, EXAFS modelling is used and the results are cross-checked with the resultant RMC simulations. EXAFS data is processed and the corresponding spectra is extracted by ATHENA software [110]. K-range is determined as $2.9\,\text{Å}^{-1}$ to $11\,\text{Å}^{-1}$, then Fourier transformed radial distance data is limited as $1.51\,\text{Å}$ to $3.45\,\text{Å}$ covering only the main amorphous peak. Photo electron scattering amplitudes extracted by $FEFF9$ software using the atomic model of the Tb-Ag-Al system [119, 120]. Coordination number and bond distances of Al atoms around Tb atoms are calculated by floating parameters of E_0, energy shift; Δ_R, interatomic path length change relative to the initial path length; σ^2, mean squared relative displacement; N, coordination number and assuming the amplitude reduction factor as 0.73 which is an accurate assumption for rare-earth metals in the absence of reference material [45, 121–124]. The goodness of fit (R_{factor}) is found to be 0.0037. CN is 15 ± 0.89 and R_{Tb-Al} is 3.06 which are in very well agreement with the RMC results, other fitting parameters are found to be E_0 as -0.95 ± 0.47, Δ_R as 0.24 ± 0.0068 and σ^2 as 0.017 ± 0.001. Correlations between the variables are well within acceptable limits. Longer range correlations structurally revealed by analyzing how certain types of clusters interact with each other. Interactions of 10 most populated Voronoi cells within themselves revealed that there are two types of clusters in the structure: network clusters of much higher size extending beyond the simulation cell regardless of the simulation cell position and separate clusters in between the branches of the network clusters that can fit in a single simulation cell depending on the position of the cell due to periodic boundary conditions. Fig. 6 (a) and (b) shows <0,2,8,5> clusters, (c) and (d) the network clusters, (e) and (f) the separate clusters for the ribbon and sputtered samples, respectively.
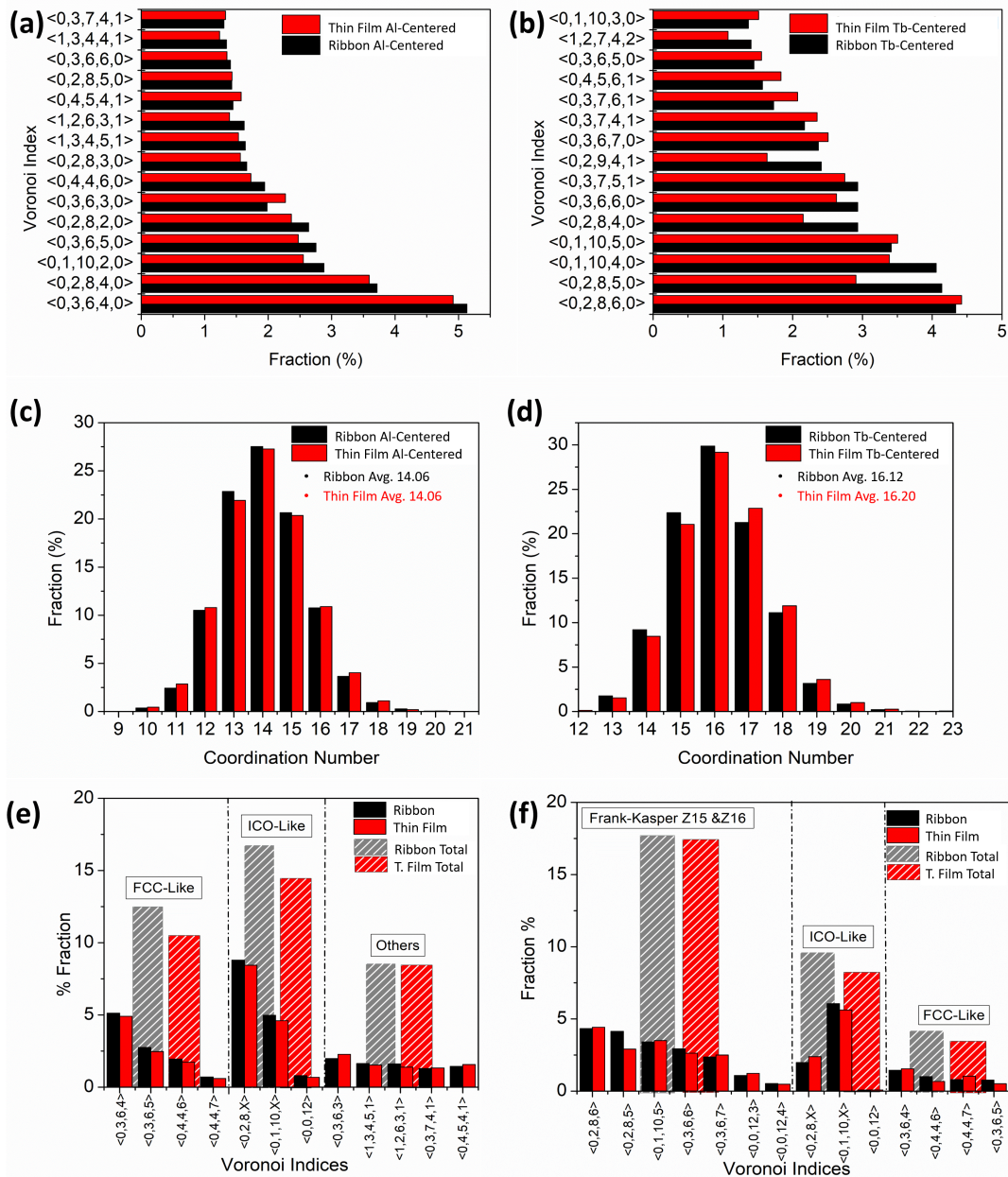
Figure 2.4: 15 most populated Voronoi cells of melt-spun ribbon and magnetron sputtered film for (a) Al centered cells and (b) Terbium centered cells, Coordination number distribution of melt-spun ribbons and magnetron sputtered films around (c) Al atoms and (d) Tb atoms, most populated Voronoi cells categorized under the structures that they resemble of for (e) Al centered and (f) Tb centered atoms.
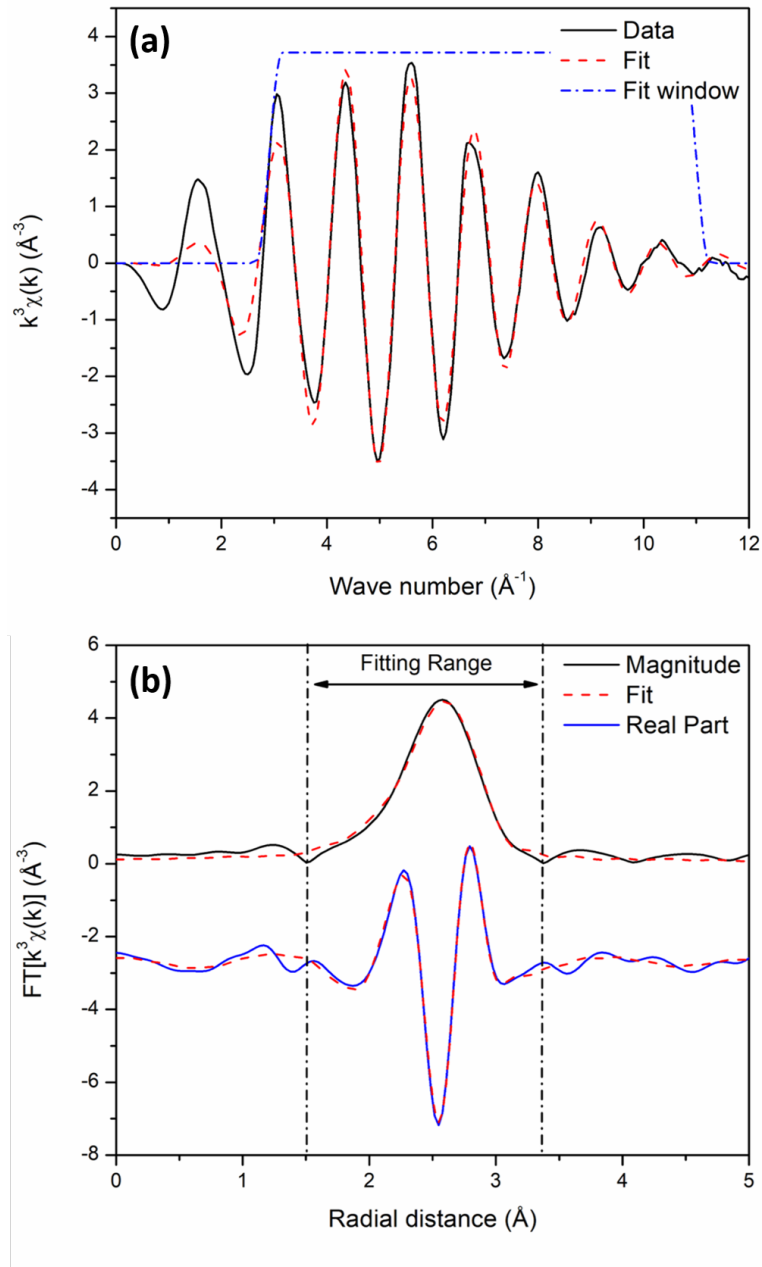
Figure 2.5: (a) Tb L_3 edge EXAFS data of $Al_{90}Tb_{10}$ melt-spun ribbon, inversed Fourier transformed in k-space and (b) Fourier transformed in r-space.

Ten most populated VPs dominating the structure are analyzed and the results are categorized under the three most pronounced structures in Table 2.1 and 2.2 for ribbon and sputtered samples. Regardless of the Voronoi cell type, atoms in ribbon form bigger network cluster and smaller number of separate clusters than atoms in thin-

film. Thin-film samples have a smaller number of atoms in overall, however they form bigger number of clusters which indicates a more disordered structure on a larger scale for three types of structures indicated in Table 1 and Table 2.

Another point of interest is the pure Al clusters. These clusters are derived from the whole simulation box by removing all the terbium atoms with their first shell neighbors. This guarantees that Al atoms that are only in contact with other Al atoms are left in the simulation box. These atoms also form clusters of various sizes. 5 biggest clusters of ribbon and sputtered samples are given in Figure 2.6. There are 33 atoms at the center of fcc-like VPs, with the addition of first shell neighbor this number goes up to 120 (45%) atoms in total of 263 atom system for ribbon. For sputtered sample there are 23 atoms at the center of fcc-like VPs, added with first neighbor shell going up to 87 (%34) atoms in a 253 atoms system. Just as in the previous cluster analyses, pure Al cluster also has a more ordered structure in ribbons. The percentage of fcc-like clusters is higher in ribbon, as well.

Table 2.1: Cluster analysis with corresponding number of atoms for the three most pronounced structures of ribbon sample.

Structure	Total # of Clusters	Total atoms	Network cluster atoms	Separate cluster atoms
Ico-like	97	35356	32310	2506
			92.80%	7.20%
Fcc-like	24	31144	30515	629
			97.98%	2.02%
Frank Kasper Type Z15 & Z16	74	19847	17460	2387
			87.9%	12.03%

Figure 2.6: (a) and (b) cluster analysis of <0,2,8,5> Voronoi cells, (c) and (d) network clusters, (e) and (f) separate clusters for melt-spun ribbon and magnetron sputtered film respectively. Pu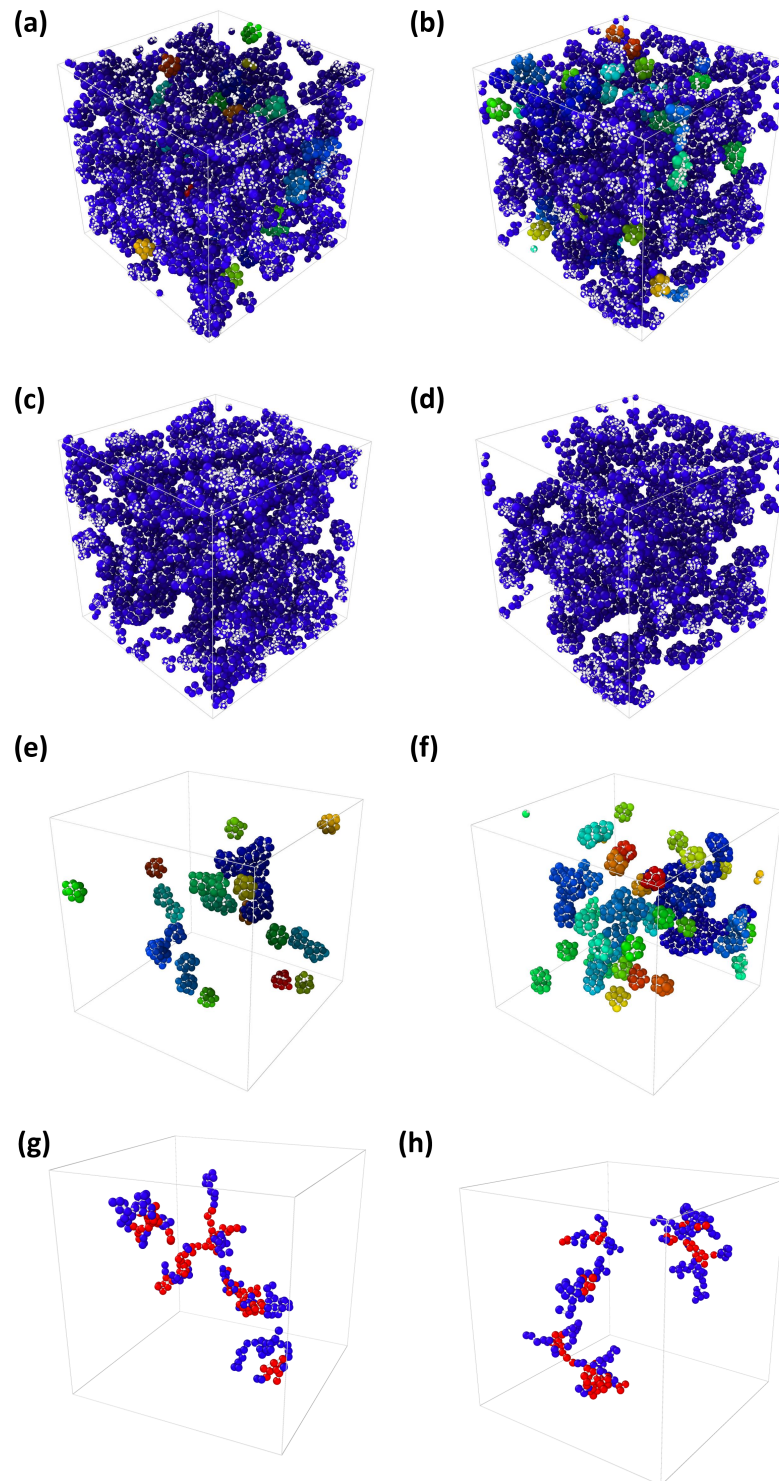re Al clusters in the structure for (g) melt-spun ribbon and (h) magnetron sputtered films, fcc-like cluster atoms (red) others (blue)

Table 2.2: Cluster analysis with corresponding number of atoms for the three most pronounced structures of thin-film sample.

Structure	Total # of Clusters	Total atoms	Network cluster atoms	Separate cluster atoms
Ico-like	104	32733	29528	3205
			90.21%	9.79%
Fcc-like	37	30139	29984	852
			97.24%	2.76%
Frank Kasper Type Z15 & Z16	89	19990	17239	2751
			86.24%	13.76%

Figure 2.7 shows the TEM images of melt-spun and sputtered thin-films in as-quenched and partially devitrified conditions. In as-quenched conditions ribbon and thin-film specimens are fully amorphous, as shown in Figure 2.7. The initial crystallization product of both specimens is fcc-Al during continuous heating as it was also detected in XRD studies. However, a major difference between ribbon and thin-film is the morphology, size and distribution of fcc-Al nanocrystals. In the case of melt-spun ribbons, fcc-Al nanocrystals are highly dendritic and gathered together as shown in Figure 2.7. Sputtered thin-films, on the other hand, devitrifies to spherical fcc-Al nanocrystal which are well separated even at lower magnifications, as shown in Figure 2.7. This is also confirmed by SAD patterns collected at similar magnification (Figure 2.7). The fcc-Al reflections in the case of melt-spun ribbons are in the form of discrete spots, however, in sputtered thin-films they are continuous rings. This clearly indicates that fcc-Al grains are much finer in sputtered thin-film as compared to melt-spun ribbon. We believe that the difference in fcc-Al nanocrystallization behavior is directly related to the as-quenched structures. As previously indicated, independent of Voronoi cell type, atoms in ribbon form bigger network cluster and smaller number of separate clusters as compared to the atoms in thin-film. Moreover, when the pure Al regions are investigated, ribbons have a higher percentage of fcc-like clusters. This shows that topological and chemical ordering in melt-spun ribbons is

higher as compared to thin-films. Thin-films quenched from vapor phase with a much higher cooling rate displays a relatively random distribution of Al-rich clusters. On the other hand, in melt-spun ribbons the sizes of the Al-rich clusters are larger with higher ordering. Upon heating, well separated fcc-Al nuclei are formed in thin-films. This was also previously confirmed by calculating the number of nucleation density of fcc-Al nanocrystals. In thin-films the population of fcc-Al nanocrystal reaches up to $10^{24}\,\mathrm{m^{-3}}$, however in melt-spun ribbon this value is measured as $10^{21}\,\mathrm{m^{-3}}$ [109]. Three order of magnitude difference in number of nucleation density also affects the morphology of the grown crystals. The rejection of Tb atoms from highly scattered Al-rich domains during crystallization causes a severe impingement in sputter thin-films which results in restricted growth of nanocrystals. The very same effect also causes the morphology of nanocrystals stay as spheres in thin-films. On the other hand, the impingement is less effective as Al-rich domains are larger and far apart. In this case, fcc-Al grains grow into larger dendrites. The size and distribution of Al-rich domains also effect the crystallization temperature. This is shown in Figure 2.8. The peak temperatures of first exothermic reaction indicating the crystallization of fcc-Al in sputtered thin-films and melt-spun ribbons are measured as $480\,\mathrm{K}$ and $530\,\mathrm{K}$, respectively. By calculating the activation energies for the fcc-Al phase transformation by Kissinger and Ozawa approaches as given in Figure 2.8, ribbons were found to have a higher activation energy by a difference of $\approx 84\,\mathrm{kJ\,mol^{-1}}$ as given in Table 3. These measurements are in good agreement with the atomic configurations of amorphous ribbon and thin-films. The higher population of Al-rich domains with relatively smaller domain size in sputtered thin-films drives the threshold of fcc-Al crystallization to lower temperature with much smaller activation energy. By analogy this resembles to supercooling observed in melting of colloidal nanocrystals. The shape and size of nanocrystals affect several thermodynamic properties including the magnitude of melting point [125]. In that sense, the activation energy of crystallization and crystallization temperature of fcc-Al in sputtered thin-films, is considerably different than the one in melt-spun ribbon specimens. The difference in local topological and chemical ordering in ribbon and thin-film amorphous structures drives the system into a diversification in crystallization behavior during devitrification.
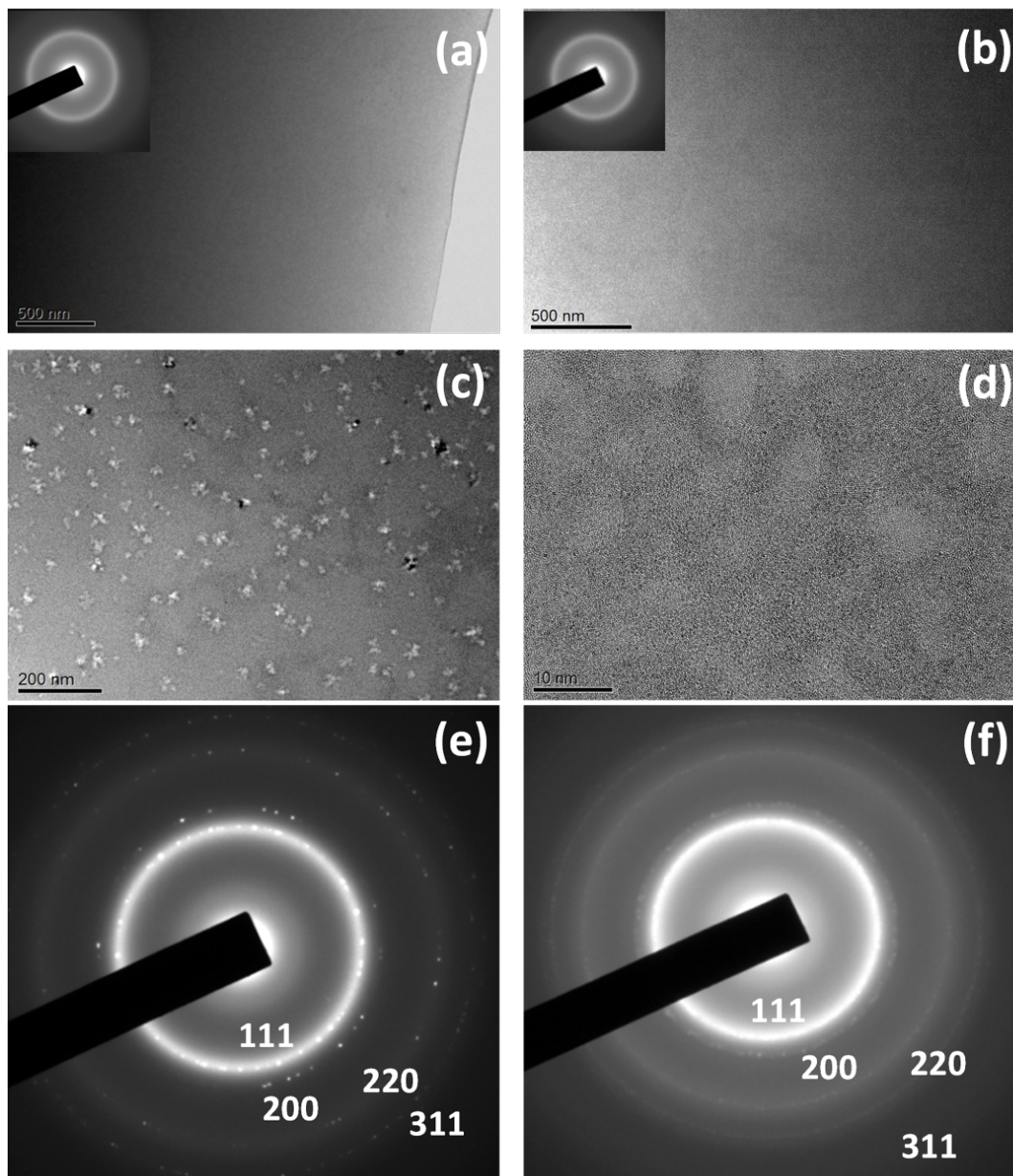
Figure 2.7: (a, b) Bright-field images and corresponding SAD patterns (in-sets), (c, d) bright-field images and (e, f) SAD after initial crystallization of as-quenched ribbon and thin-film $Al_{90}Tb_{10}$, respectively. SAD indexing represents fcc-Al reflections.
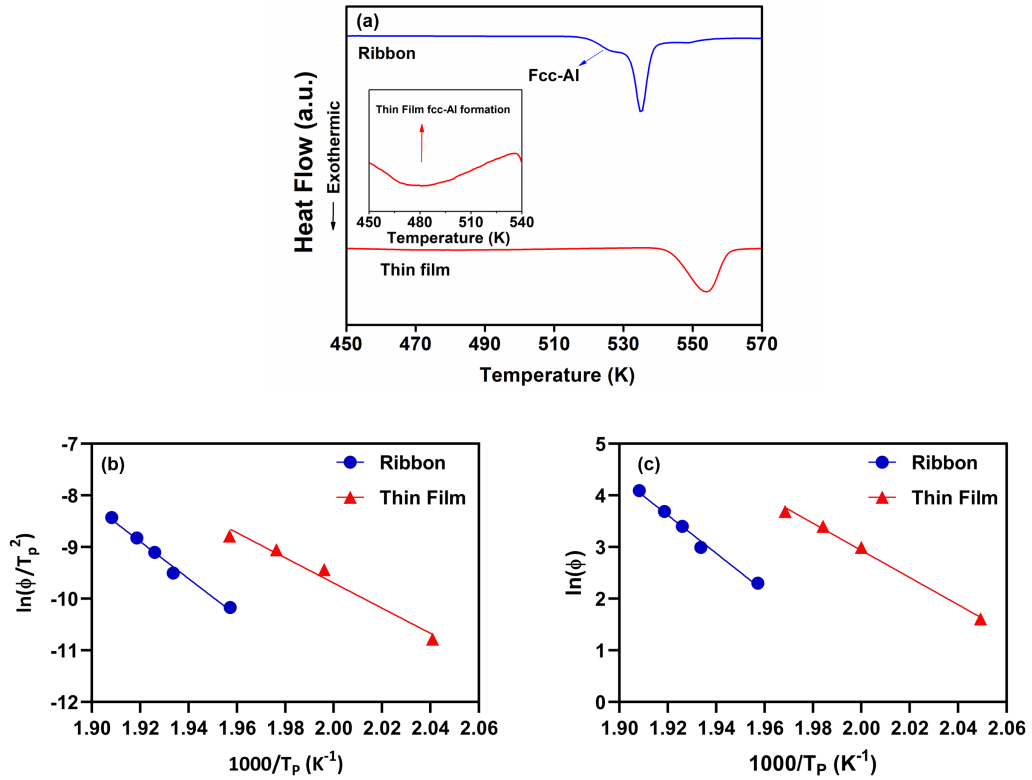
Figure 2.8: ((a) Continuous DSC traces for melt-spun ribbons and sputtered thin-films collected at 40 K/min heating rate (b)Kissinger and (c) Ozawa plots.

Table 2.3: Activation energies for the crystallization of fcc-Al phase by Kissinger and Ozawa analysis

Structure	Kissinger Ec kJ/mole	Ozawa Ec kJ/mole
Ribbon	298 ± 1	291 ± 2
Thin Film	210 ± 1	207 ± 2

2.4 Conclusion

The effects of amorphous structure in melt-spun ribbon and sputtered thin-film on nucleation and growth behavior of fcc-Al nanocrystals were comprehensively inves-

tigated by a combination of electron and X-ray oriented characterization techniques in $Al_{90}Tb_{10}$ metallic glasses. EXAFS, HEXRD and ab-initio constrained RMC results showed that melt-spun alloys have a higher degree of short-range order than sputtered thin-films. Clustering of the atoms with respect to their Voronoi cell structures is also different as ribbons forming larger clusters of similar atomic structures whereas thin-films forming smaller, scattered and disordered clusters. Pure Al clusters in the structure are considered to be nucleation domains for fcc Al crystals upon heating. Analyzing the five biggest clusters for both samples revealed that despite having similar sizes, ribbon samples have a significantly higher percentage of fcc-like structures than the thin-film samples. TEM investigations are in good agreement with RMC simulations. The fcc-Al nanocrystals nucleated and grown in thin-film specimens have limited size with almost perfect spherical morphology. The population of these nanocrystals is three order of magnitude higher as compared to ribbon specimens. The thermal analyses revealed that the energy barrier for nucleation of the first fcc crystals is significantly lower for thin-film specimens. Which is originated from the order wise differences inherited from the parental liquid and gaseous phases. The main reason for the diversification in crystallization behavior is that ribbon form larger and well separated pure Al regions than the thin-film. Which in turn lowers the activation barrier and crystallization temperature of thin-film samples. This structural difference is believed to be originated from inhomogeneities in liquid state.

2.5 Acknowledgements

CHAPTER 3

MECHANICAL EVALUATION OF AL-TB MICROPILLARS

3.1 Introduction

Correlating the structural attributes with properties have been the main objective in materials engineering and research. Main route followed to accomplish this have been determining the structural components and defects for crystalline materials. Structural components and defects for crystalline materials are very well defined. Also characterization methods to analyze these attributes are vast and very well established. However this is not the case for amorphous materials and especially metallic glasses. Since there are not well defined components of metallic glasses, in fact most of the time it is not possible tell two amorphous structures of metallic glasses apart. Describing and most importantly quantifying methods for structural attributes are much harder and not well established. Finally experimental and computational requirements for metallic glasses are nowhere near their crystalline counterparts.

Nonetheless, there are promising studies that include both experimental and computational solutions to these problems that will ultimately enable us to reveal the structural attributes of metallic glasses and correlate with their properties [126]. Due to size restrictions mechanical tests are mainly performed on micropillars via compression tests. However there are certain concerns on how micropillar size and tapper angel affect the results [127, 128]. It is stated that larger sample diameter increases the strain bursts and therefore alloy becomes brittle [129, 130]. Fe based metallic glasses seem to have strain bursts that last the longest while Zr based metallic glasses are the shortest. This means Zr based are more ductile since larger strain bursts are characteristics of brittleness [127]. Where as tapper angle of $5°$ seems to be highest limit

for measurement since higher angles result is higher yield strength [131]. Plasticity on single crystals study constructed the micro force balance phenomena [132] which was coupled with thermodynamics principles and used to develop a model for finite element analysis [133]. This study can simulate the stress strain behavior of metallic glasses reasonably well. Later on effect of intrinsic length scale during shear band formation was modeled for below micron size metallic glasses [134].

In this study marginal metallic glass system $Al_{90}Tb_{10}$ system was studied through a series of DSC and micropillar compression tests. DSC was used to impart different amounts of nanocrystallibity into amorphous matrix. focused ion beam milling (FIB) was used to fabricate micropillars where micropillar compression tests were performed. Stress-strain diagrams and fractures surfaces were then analyzed to see how ductility and fractures stress changes from fully amorphous sample to FCC nanocrystal and intermetallic embedded structure.

3.2   Experimental

$Al_{90}Tb_{10}$ melt-spun ribbons mentioned in chapter were used for micro pillar fabrication, DSC measurements, micro pillar compression tests and TEM analysis. Five type of samples were prepared for fully amorphous, $241\,°C$, $251\,°C$, $259\,°C$, $263\,°C$ annealed samples.

DSC measurements were done on $1\,mg$ to $1.6\,mg$ samples of $Al_{90}Tb_{10}$ melt-spun ribbons with empty Al pans used as references. Samples were heated from room temperature up to desired temperatures at $40\,°C\,min^{-1}$ and cooled down to room temperature at $100\,°C\,min^{-1}$ under protective N_2 atmosphere.

Micropillars of $2.75\,$top surface diameter, $3\,\mu m$ medium height diameter and $3.25\,\mu m$ bottom diameter are fabricated on melt-spun ribbons via FIB. Micropillar compression tests were then performed on these micropillar and stress-strain diagrams are extracted. Compression tests were performed in displacement controlled mode with linear loading and unloading stages. Three different loading rates were applied which corresponded to strain rates around 10^{-2}, 10^{-4} and 10^{-5} 1/s.

3.3 Results and Discussion

DSC traces of the $Al_{90}Tb_{10}$ sample given in Figure 3.1 shows the structural changes accompanied by heating from room temperature up to $500\,°C$.
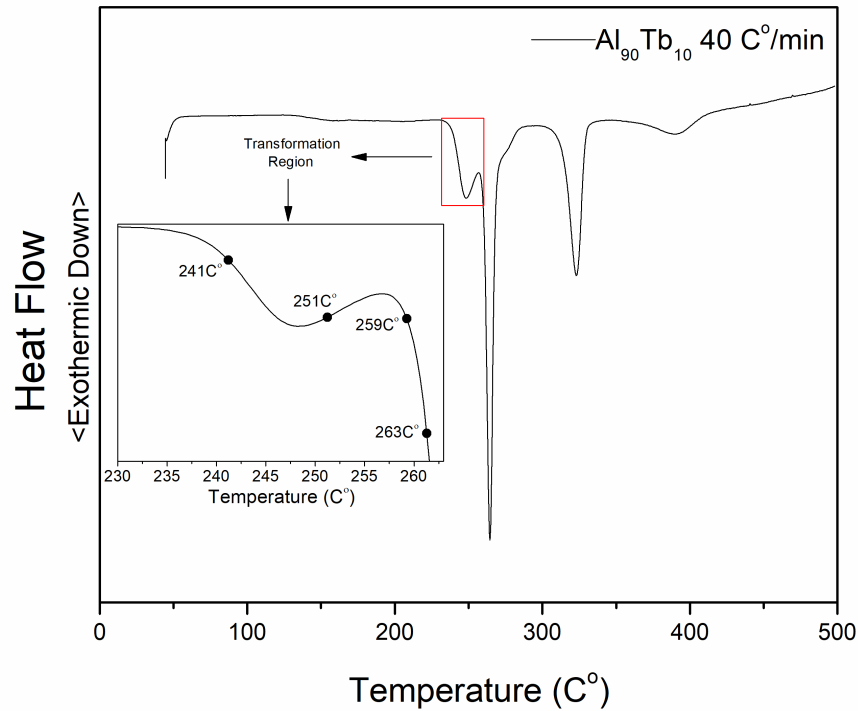
Figure 3.1: Differential scanning calorimetry traces of $Al_{90}Tb_{10}$ samples. Inset showing the annealing temperatures in the first FCC Al crystallization and second the intermetallic compound formation.

First exothermic peak labeled as transformation region starting from around $230\,°C$ is the FCC Al nanocrystal formation region. End of this transformation peak coincides with the start of second peak which is the intermetallic formation region and 3rd peak is also another intermetallic formation which is out of topic for this study. Four heat treated samples out of five are chosen as $241\,°C$ as start of the FCC Al crystallization, $251\,°C$ deeper into FCC Al region, $259\,°C$ end of FCC Al and start of intermetallic region and finally $263\,°C$ deeper in to intermetallic region.

Figure 3.2: Al$_{90}$Tb$_{10}$ fully amorphous (a) Stress strain diagram of 4 samples, (b), (c), (d) and (e) SEM images of micro pillars and fracture surfaces.

Fully amorphous non-heat treated sample as a reference is given in Figure 3.2. Micropillars before and after deformation given shows that the samples were broken in a brittle manner with serrated flow starting from lower stress values with 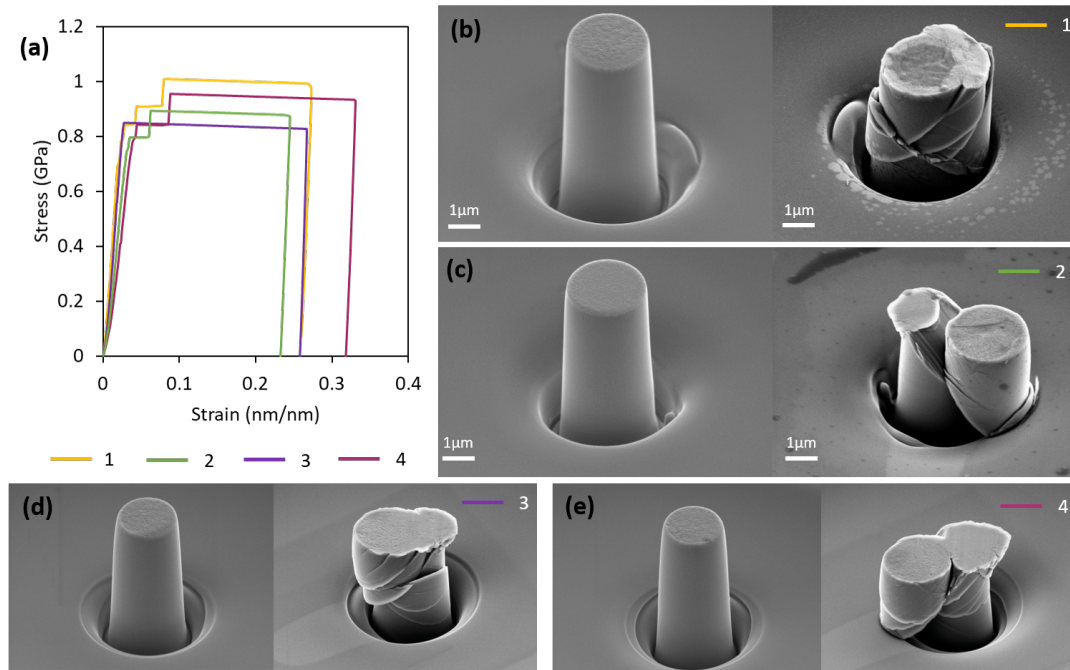smaller strain bursts. As stress increase strain bursts become wider and longer. Fracture stress for these samples is about $0.9\,\text{GPa}$. Brittle nature of the samples can also be observed from the SEM images deformed micro pillars. Multiple shear bands formed are at around $45°$ and almost all shear bands starts and extends through the sample. These are the characteristics of faster shear band propagation and hence more catastrophic, brittle failure as shown in Figure 3.2.

Samples heat treated at $241\,°\text{C}$ show an increase in fractures stress. Following the introduction of nanocrystals fractures stress goes beyond $1\,\text{GPa}$. Also there is an increase in the amount of smaller shear bursts in the low stress region and a decrease in the amount of big shear bursts. This behavior is considered to be a result of shear bands not being able to find area to grow before they get intercepted by crystals. Similar results can be seen by SEM images of fracture surfaces as well. There is a noticeable decrease in the amount of big shear band cracks that extends through the

48

sample as shown in Figure 3.3.

Samples heat treated at $251\,°\mathrm{C}$ show similar beahvior as fracture stress continue to rise up to $1.2\,\mathrm{GPa}$. Accompanied by the increased amount of nanocrsytals introduced in amorphous matrix small shear burst region in low stress values becomes more ductile and as in the $241\,°\mathrm{C}$ heat treated samples only one or two big shear bursts prior to failure at high stress values. SEM images of the fracture surfaces show the one big shear burst that that extends through the samples causing the failure accompanied smaller shear bursts as shown in Figure 3.4.

Figure 3.3: $Al_{90}Tb_{10}$ $241\,°\mathrm{C}$ heat treated (a) Stress strain diagram of 3 samples, (b), (c) and (d) SEM images of micro pillars and fracture surfaces.

Figure 3.4: $Al_{90}Tb_{10}$ 251 °C heat treated (a) Stress strain diagram of 4 samples, (b) and (c) SEM images of micro pillars and fracture surfaces.

Figure 3.5: $Al_{90}Tb_{10}$ 259 °C heat treated (a) Stress strain diagram of 3 samples, (b) and (c) SEM images of micro pillars and fracture surfaces.

As heat treatment temperature increases to 251 °C intermetallic compound formation starts, fracture stress increase comes to an end. Smaller shear bursts in the low stress regions cease to exist as shown in Figure 3.5.
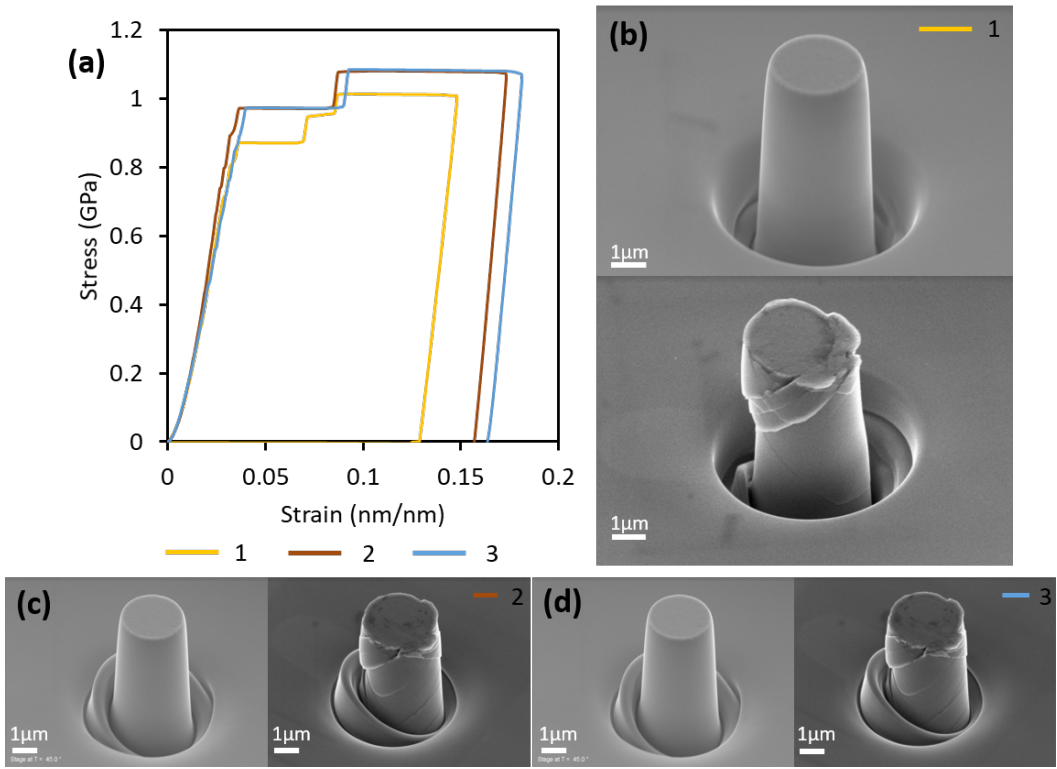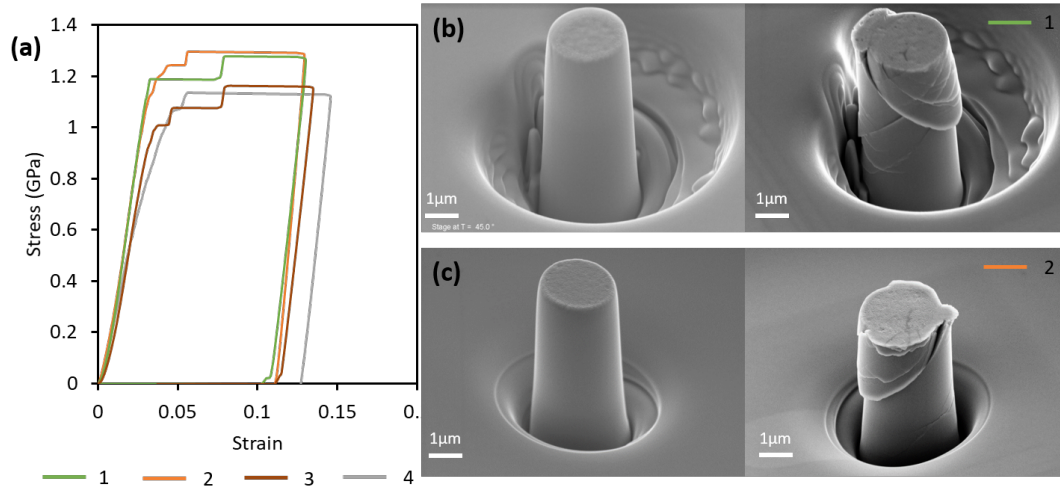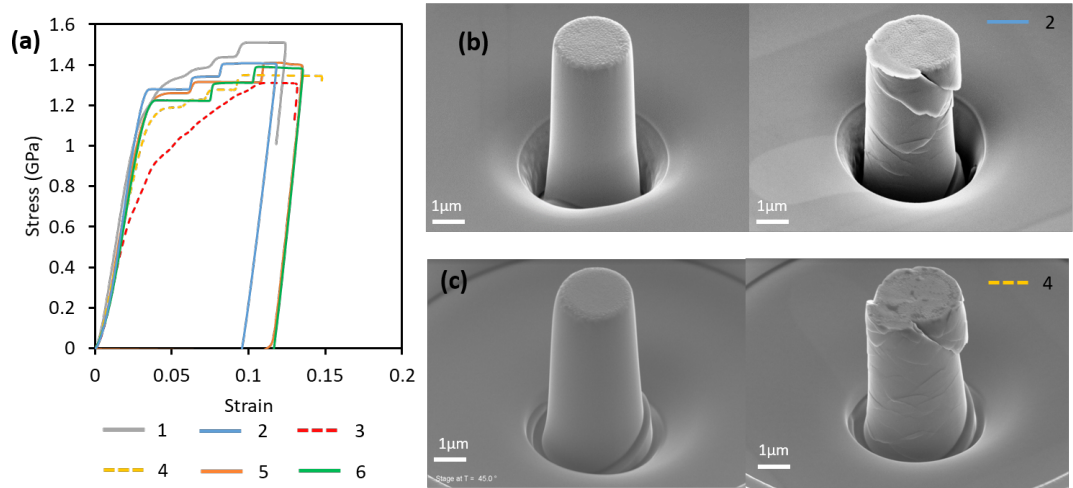
Figure 3.6: $Al_{90}Tb_{10}$ $263\,°C$ heat treated (a) Stress strain diagram of 6 samples, (b) and (c) SEM images of micro pillars and fracture surfaces.
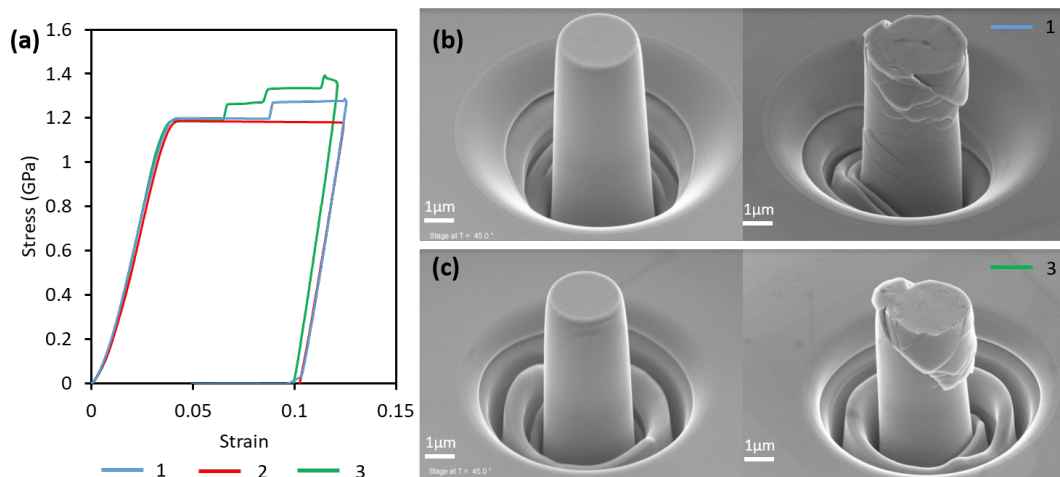
Heat treatment up to intermetallic formation temperature results in increase in fracture stress however small strain bursts are almost completely gone and there is a slight increase in big strains which indicates an increase in brittleness as expected since intermetallic compounds of Al and Tb are extremely brittle.

3.4   Conclusion

Metallic glasses are considered for structural applications but their brittleness and catastrophic failure have been the main obstacle. Mechanical properties of $Al_{90}Tb_{10}$ system were studied by DSC iniated heat treatment where nanocrystals and inter-metallic compounds were embedded in the amorphous matrix. Micropillar compression test was applied due to sample size restrictions. It has been seen that introduction of FCC Al nanocrystals have made considerable improvements in both fracture stress and ductility, overcoming the ductility vs. strength trade off. This is considered to be achieved by restricting the movement of shear bands at nanocrystals. Addition of in-termetallic compound however raises some concerns. Although fracture stress shows a noticeable increase, samples starts to show brittle characteristics back again.

51

3.5 Acknowledgments

CHAPTER 4

CONCLUSIONS AND FUTURE RECOMMENDATIONS

4.1 Conclusions

In this study the structural analysis, abnormal crystallization behavior and mechanical properties of fully amorphous, partially crystallized $Al_{90}Tb_{10}$ marginal glass former alloys produced via melt spinning and magnetron sputtering were studied. Study covers the controversial topics in structural analysis, crystallization and relatively less studied mechanical properties of Al based marginal glass formers.

Previously found models on $Al_{90}Tb_{10}$ system [42,109] was improved with RMC modelling where two experimental data sets of HEXRD, XAFS and computational parameters obtained from Ab-initio simulations used. Results were checked with EXAFS modelling to remove deficiencies of RMC method. Created model was studied with Voronoi tessellation in short range and cluster analysis. Nature of abnormal crystallization behavior revealed. RMC results showed that melt-spun alloys have a higher degree of order than sputtered thin-films. Clusters of pure Al identified by Voronoi analyses were found to be smaller and spatially scattered in thin-film specimens as compared to melt-spun ribbons. Analyzing the five largest clusters for both conditions revealed that ribbon samples have a significantly higher percentage of fcc-like structures than the thin-film samples. These pure Al clusters embedded in the structure are considered to be the nucleation domains for fcc Al crystals upon heating. TEM investigations are in good agreement with RMC simulations. The fcc-Al nanocrystals nucleated and grown in thin-film specimens have a limited size with almost perfect spherical morphology. The population of these nanocrystals is three orders of magnitude higher as compared to ribbon specimens. The thermal analyses revealed that

the energy barrier for nucleation of the first fcc crystals is significantly lower for thin-film specimens. The spatially well separated domains cause that the energy barrier for nucleation of the first fcc crystals is significantly lower for thin-film specimens. As the fcc-Al nanocrystals grow further, the rejected Tb atoms cause an aggressive soft impingement in thin-films which restricts the size of individual fcc-Al nanocrystals to stay less than $50\,\text{nm}$.

Mechanical testing part covers the effects of partial crystallization on mechanical properties of $Al_{90}Tb_{10}$ system. Micropillars formed by FIB milling was compressed via micropillar compression tests. Results revealed that embedding nanocrystals to amorphous matrix increases both fracture stress and ductility. However increasing the annealing temperature enables intermetallic formation which decreases ductility while increasing fracture stress.

4.2 Future Recommendations

Al based marginal glass formers were studied in length in literature due their intriguing structure and superior properties. Many questions regarding the structure and how it affects the properties were answered. However there is still no clear answer on how these structures form, why there is an abnormal nucleation behavior and finally the deformation mechanisms in partially crystallized systems is less known.

In order to answer these questions there are two studies going on in SML laboratory. First study focuses on liquid state characterization of marginal glass formers in and out of glass formation range. Al-Tb system for example, phase diagram given in Figure 4.1 forms glass in $9 - 14$ at.% beyond eutectic composition where it reaches much higher undercooling. Whereas other metallic glasses have GFR in eutectic compositions. We believe that the RE elements forms a network in which the structure is divided into pure Al regions and at the GFR compositions these regions are below the critical nucleation size and consecutively can reach much higher undercooling.

Second study focuses on the mechanical aspects and builds on the results of third chapter. In order to better understand how embedding increases both ductility and fracture stress it is crucial to understand the deformation mechanism in partially crys-
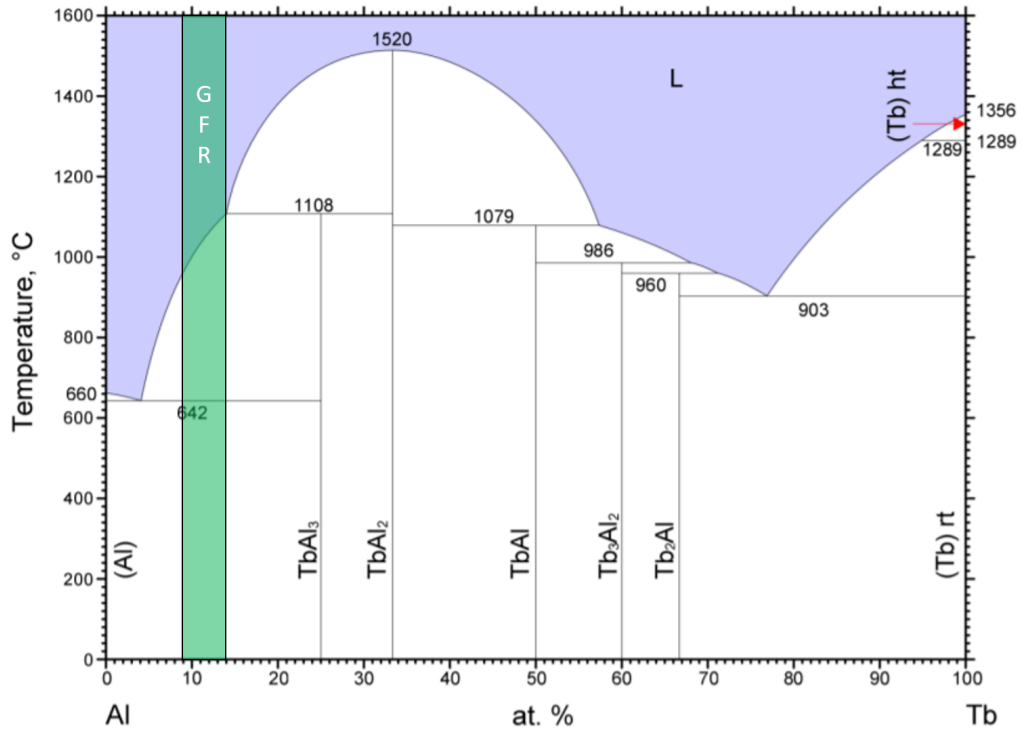
Figure 4.1: Al-Tb phase diagram, GFR is highlighted green.

tallized metallic glasses. Aim of this study to do HRTEM analysis on shear bands formed in micropillars during compression. So far TEM samples for fully amorphous and 251 °C heat treated samples were prepared by FIB milling. Micro pillars were deposited with Pt to protect the pillar region and milled from front and back end until a section of desired thickness were achieved for HRTEM as given in Figure 4.2.

Primary HRTEM results have interesting features on how shear bands form and proceeds through the amorphous matrix, how they react with nanocrystals and leaves the crystals and return to amorphous matrix as given in Figure 4.3 for fully amorphous sample and Figure 4.4 for 251 °C heat treated sample. However in order to have the whole picture on the mechanism of deformation more TEM analysis should be done on various strain bursts both small and large to see how ductile deformation and final brittle fracture takes place.

55

Figure 4.2: (a) Pt deposition on micro pillar, (b) primary thinning and (c) final HRTEM sample

Figure 4.3: (a) Bright field image of whole micropillar, (b) Bright field image of shear region and (c) HRTEM image of shear band for fully amorphous sample.
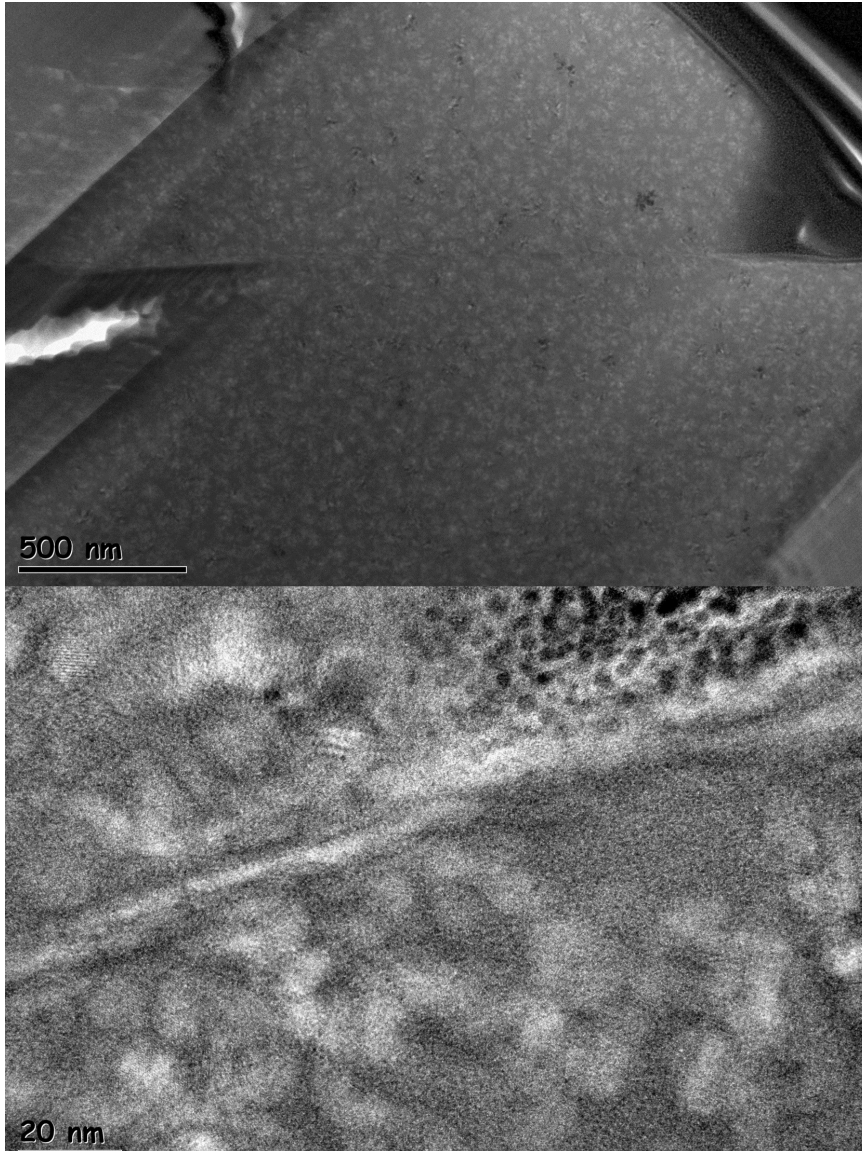
Figure 4.4: (a) Bright field image of whole micropillar, (b) HRTEM image of shear region and (c) HRTEM image of shear band for 251 °C heat treated sample.

REFERENCES

[1] S. R. Elliott, "The Structure of Amorphous Materials," in *Properties and Applications of Amorphous Materials*, pp. 1–11, Springer Netherlands, 2001.

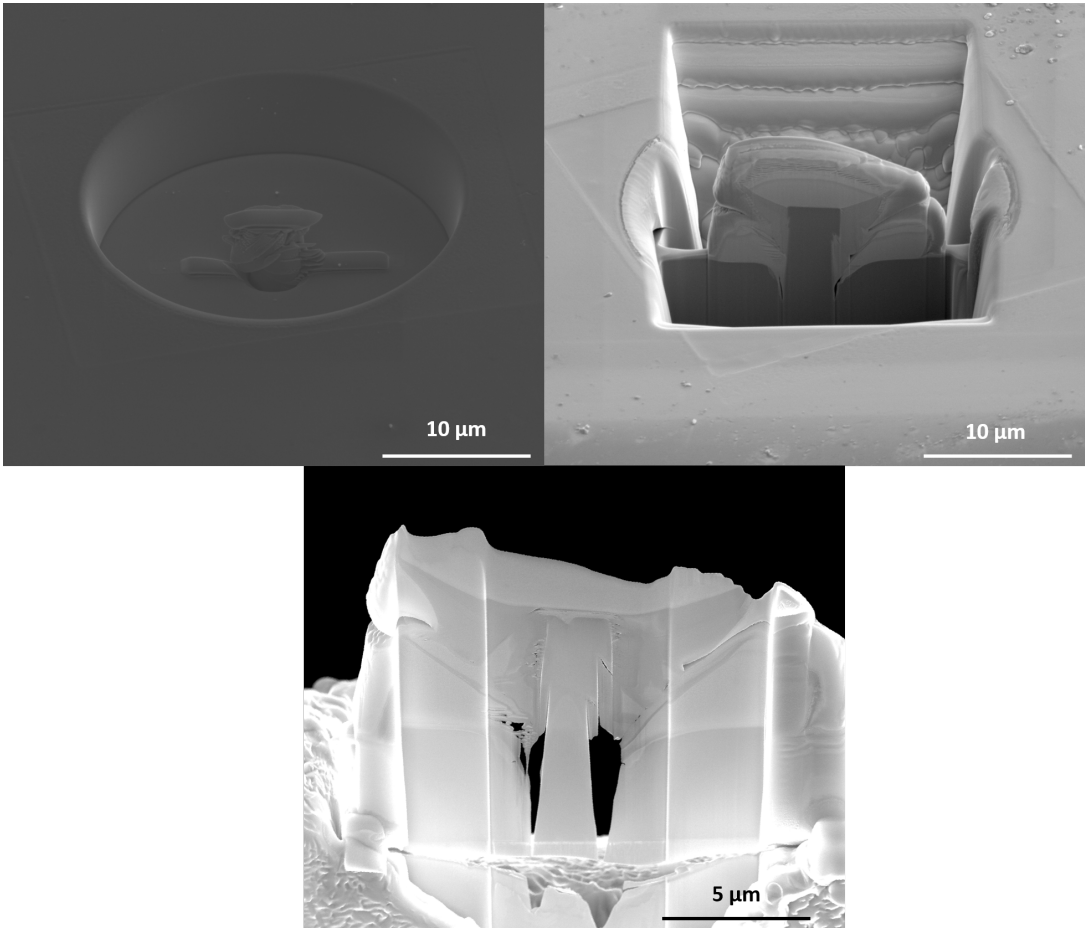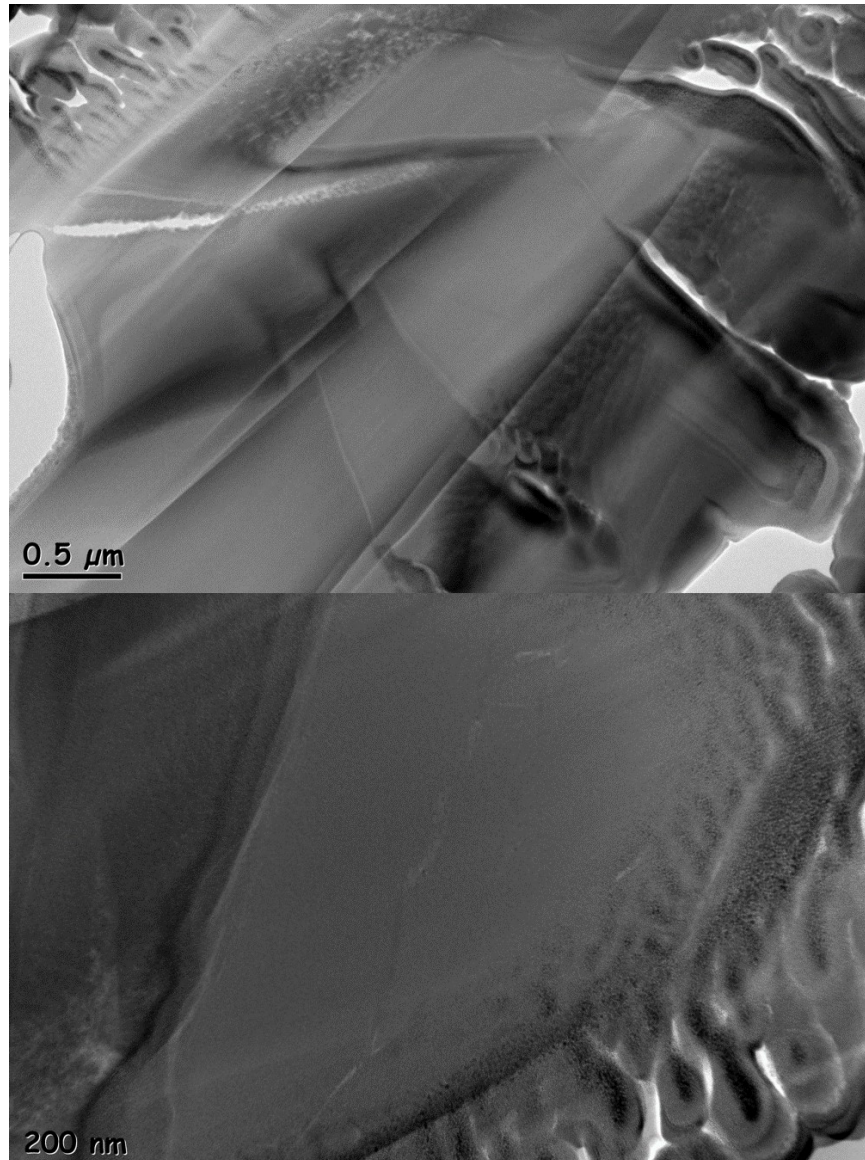[2] C. D. Conner, " Science and Technology in World History: An Introduction , by James T. McClellan III and Harold Dorn. Science and Technology in World History: An Introduction , by James T. McClellan III and Harold Dorn. Baltimore, Maryland, Johns Hopkins University Pres," *Canadian Journal of History*, vol. 35, pp. 401–403, aug 2000.

[3] C. C. Lamberg-Karlovsky and P. R. S. Moorey, "Our Past Matters: Materials and Industries of the Ancient Near EastAncient Mesopotamian Materials and Industries: The Archaeological Evidence," *Journal of the American Oriental Society*, vol. 117, p. 87, jan 1997.

[4] W. Klement, R. H. Willens, and P. Duwez, "Non-crystalline structure in solidified Gold-Silicon alloys," *Nature*, vol. 187, no. 4740, pp. 869–870, 1960.

[5] H. S. Chen, "Glassy metals," *Reports on Progress in Physics*, vol. 43, no. 4, pp. 353–432, 1980.

[6] A. L. Greer, "Metallic glasses," *Science*, vol. 267, no. 5206, pp. 1947–1953, 1995.

[7] W. L. Johnson, "Bulk glass-forming metallic alloys: science and technology," *MRS Bulletin*, vol. 24, no. 10, pp. 42–56, 1999.

[8] A. Inoue, "Stabilization of metallic supercooled liquid and bulk amorphous alloys," *Acta Materialia*, vol. 48, pp. 279–306, jan 2000.

[9] A. Inoue and A. Takeuchi, "Recent progress in bulk glassy alloys," *Materials Transactions*, vol. 43, no. 8, pp. 1892–1906, 2002.

[10] W. L. Johnson, "Bulk amorphous metal-An emerging engineering material," *JOM*, vol. 54, no. 3, pp. 40–43, 2002.

[11] J. F. Löffler, "Bulk metallic glasses," jun 2003.

[12] W. H. Wang, C. Dong, and C. H. Shek, "Bulk metallic glasses," *Materials Science and Engineering R: Reports*, vol. 44, pp. 45–89, jun 2004.

[13] A. L. Greer and E. Ma, "Bulk Metallic Glasses: At the Cutting Edge of Metals Research," *MRS Bulletin*, vol. 32, pp. 611–619, aug 2007.

[14] A. L. Greer, "Metallic glasses...on the threshold," jan 2009.

[15] A. Inoue, "Bulk Glassy Alloys: Historical Development and Current Research," *Engineering*, vol. 1, pp. 185–191, jun 2015.

[16] Y. Cheng and E. Ma, "Atomic-level structure and structure–property relationship in metallic glasses," *Progress in Materials Science*, vol. 56, pp. 379–473, may 2011.

[17] C. Fan, X. Yue, A. Inoue, C.-T. Liu, X. Shen, and P. K. Liaw, "Recent Topics on the Structure and Crystallization of Al-based Glassy Alloys," *Materials Research*, vol. 22, feb 2019.

[18] A. Inoue, A. Kitamura, and T. Masumoto, "The effect of aluminium on mechanical properties and thermal stability of (Fe, Co, Ni)-Al-B ternary amorphous alloys," *Journal of Materials Science*, vol. 16, pp. 1895–1908, jul 1981.

[19] R. O. Suzuki, Y. Komatsu, K. F. Kobayashi, and P. H. Shingu, "Formation and crystallization of Al-Fe-Si amorphous alloys," *Journal of Materials Science*, vol. 18, pp. 1195–1201, apr 1983.

[20] A. Inoue, Y. Bizen, and T. Masumoto, "Quasicrystalline phase in Al-Si-Mn system prepared by annealing of amorphous phase," *Metallurgical Transactions A*, vol. 19, pp. 383–385, feb 1988.

[21] A. Inoue, K. Ohtera, K. Kita, and T. Masumoto, "New amorphous alloys with good ductility in al-ce-m (m=nb, fe, co, ni or cu) systems," *Japanese Journal of Applied Physics*, vol. 27, no. 10 A, pp. L1796–L1799, 1988.

[22] A. Inoue, K. Ohtera, and T. Masumoto, "New amorphous al-y, al-la and al-ce alloys prepared by melt spinning," *Japanese Journal of Applied Physics*, vol. 27, no. 5A, pp. L736–L739, 1988.

[23] A. P. Tsai, A. Inoue, and T. Masumoto, "Formation of metal-metal type aluminum-based amorphous alloys," *Metallurgical Transactions A*, vol. 19, pp. 1369–1371, may 1988.

[24] Y. He, S. J. Poon, and G. J. Shiflet, "Synthesis and properties of metallic glasses that contain aluminum," *Science*, vol. 241, pp. 1640–1642, mar 1988.

[25] Y. He, S. J. Poon, and G. J. Shiflet, "Formation and stability of aluminum-based metallic glasses in Al-Fe-Gd alloys," *Scripta Metallurgica*, vol. 22, pp. 1813–1816, jan 1988.

[26] J. Henao, A. Concustell, I. G.Cano, S. Dosta, N. Cinca, J. M. Guilemany, and T. Suhonen, "Novel Al-based metallic glass coatings by Cold Gas Spray," *Materials and Design*, vol. 94, pp. 253–261, mar 2016.

[27] Y. G. Wang, Y. J. Li, S. P. Pan, B. D. Fu, J. Y. Qin, and W. M. Wang, "Role of Yttrium Substitution in the Atomic Cluster Evolution and Corrosion Behaviour of Al-Ni-Gd Metallic Glasses," *Int. J. Electrochem. Sci*, vol. 11, pp. 3512–3531, 2016.

[28] Y. He, G. J. Shiflet, and S. J. Poon, "Ball milling-induced nanocrystal formation in aluminum-based metallic glasses," *Acta Metallurgica Et Materialia*, vol. 43, pp. 83–91, jan 1995.

[29] A. P. Tsai, T. Kamiyama, Y. Kawamura, A. Inoue, and T. Masumoto, "Formation and precipitation mechanism of nanoscale Al particles in Al-Ni base amorphous alloys," *Acta Materialia*, vol. 45, pp. 1477–1487, apr 1997.

[30] C. Fan and A. Inoue, "Ductility of bulk nanocrystalline composites and metallic glasses at room temperature," *Applied Physics Letters*, vol. 77, no. 1, pp. 46–48, 2000.

[31] J. Mu, H. Fu, Z. Zhu, A. Wang, H. Li, Z. Hu, and H. Zhang, "Synthesis and Properties of Al-Ni-La Bulk Metallic Glass," *Advanced Engineering Materials*, vol. 11, pp. 530–532, jul 2009.

[32] J. J. Yi, X. Z. Xiong, A. Inoue, L. T. Kong, and J. F. Li, "Glass forming ability of Al-Ni-La alloys with Si addition," *Journal of Alloys and Compounds*, vol. 650, pp. 578–583, nov 2015.

[33] A. Inoue, N. Matsumoto, and T. Masumoto, "Al–Ni–Y–Co Amorphous Alloys with High Mechanical Strengths, Wide Supercooled Liquid Region and Large Glass-Forming Capacity," *Materials Transactions, JIM*, vol. 31, no. 6, pp. 493–500, 1990.

[34] C. T. Rios, L. C. R. Aliaga, C. S. Kiminami, C. Bolfarini, and W. J. B. Filho, "Stability of an amorphous alloy of the Mm-Al-Ni-Cu system," in *Materials Research*, vol. 15, pp. 757–762, Materials Research, sep 2012.

[35] M. Yan, S. Kohara, J. Q. Wang, K. Nogita, G. B. Schaffer, and M. Qian, "The influence of topological structure on bulk glass formation in Al-based metallic glasses," *Scripta Materialia*, vol. 65, pp. 755–758, nov 2011.

[36] B. A. Sun, M. X. Pan, D. Q. Zhao, W. H. Wang, X. K. Xi, M. T. Sandor, and Y. Wu, "Aluminum-rich bulk metallic glasses," *Scripta Materialia*, vol. 59, pp. 1159–1162, 2008.

[37] F. Q. Guo, S. J. Enouf, S. J. Poon, and G. J. Shiflet, "Formation of ductile Al-based metallic glasses without rare-earth elements," *Philosophical Magazine Letters*, vol. 81, pp. 203–211, mar 2001.

[38] K. Saksl, P. Jóvári, H. Franz, and J. Z. Jiang, "Atomic structure of Al 88Y 7Fe 5 metallic glass," *Journal of Applied Physics*, vol. 97, p. 113507, jun 2005.

[39] K. L. Sahoo and R. Sahu, "Glass transition and crystallization of Al–Ni–La based metallic glasses studied by temperature modulated DSC," apr 2013.

[40] L. A. Akashev and V. E. Sidorov, "The optical properties of Al-8 at.% Ce alloy in the liquid, amorphous, and crystalline states," *High Temperature*, vol. 47, pp. 331–335, jun 2009.

[41] a. Inoue, H. M. Kimura, K. Sasamori, and T. Masumoto, "Ultrahigh Strength of Rapidly Solidified Al96-Xcr3ci1cox (X=1, 1.5 and 2-Percent Alloys Containing an Icosahedral Phase as a Main Component," 1994.

[42] Y. E. Kalay, I. Kalay, J. Hwang, P. M. Voyles, and M. J. Kramer, "Local chemical and topological order in Al-Tb and its role in controlling nanocrystal formation," *Acta Materialia*, 2012.

[43] Y. E. Kalay, L. S. Chumbley, and I. E. Anderson, "Crystallization behavior in a highly driven marginal glass forming alloy," *Journal of Non-Crystalline Solids*, 2008.

[44] Y. E. Kalay, L. S. Chumbley, M. J. Kramer, and I. E. Anderson, "Local structure in marginal glass forming Al-Sm alloy," *Intermetallics*, vol. 18, pp. 1676–1682, aug 2010.

[45] W. Zalewski, J. Antonowicz, R. Bacewicz, and J. Latuch, "Local atomic order in Al-based metallic glasses studied using XAFS method," *Journal of Alloys and Compounds*, vol. 468, pp. 40–46, jan 2009.

[46] Y. Sun, F. Zhang, Z. Ye, Y. Zhang, X. Fang, Z. Ding, C. Z. Wang, M. I. Mendelev, R. T. Ott, M. J. Kramer, and K. M. Ho, "Crystal Genes' in Metallic Liquids and Glasses," *Scientific Reports*, vol. 6, pp. 1–8, mar 2016.

[47] Y. Sun, Y. Zhang, F. Zhang, Z. Ye, Z. Ding, C. Z. Wang, and K. M. Ho, "Cooling rate dependence of structural order in Al90Sm10 metallic glass," *Journal of Applied Physics*, vol. 120, p. 015901, jul 2016.

[48] D. B. Miracle and O. N. Senkov, "A geometric model for atomic configurations in amorphous Al alloys," *Journal of Non-Crystalline Solids*, vol. 319, pp. 174–191, may 2003.

[49] D. B. Miracle, "A structural model for metallic glasses," *Nature Materials*, vol. 3, pp. 697–702, sep 2004.

[50] D. B. Miracle, "The efficient cluster packing model - An atomic structural model for metallic glasses," *Acta Materialia*, vol. 54, pp. 4317–4336, sep 2006.

[51] N. C. Wu, D. Kan, L. Zuo, and J. Q. Wang, "Efficient atomic packing-chemistry coupled model and glass formation in ternary Al-based metallic glasses," *Intermetallics*, vol. 39, pp. 1–4, aug 2013.

[52] N. C. Wu, M. Yan, L. Zuo, and J. Q. Wang, "Correlation between medium-range order structure and glass-forming ability for Al-based metallic glasses," *Journal of Applied Physics*, vol. 115, p. 043523, jan 2014.

[53] R. I. Wu, G. Wilde, and J. H. Perepezko, "Glass formation and primary nanocrystallization in Al-base metallic glasses," *Materials Science and Engineering A*, vol. 301, pp. 12–17, mar 2001.

[54] H. Nitsche, F. Sommer, and E. J. Mittemeijer, "The Al nano-crystallization process in amorphous Al85Ni 8Y5Co2," *Journal of Non-Crystalline Solids*, vol. 351, pp. 3760–3771, dec 2005.

[55] S. Rassolov, V. Tkatch, V. Maslov, V. Maksimov, K. Svyrydova, and I. Zhikharev, "Nanocrystallization of Al-based glasses via nucleation and growth under "soft impingement" conditions," *physica status solidi (c)*, vol. 7, pp. 1340–1343, apr 2010.

[56] D. V. Louzguine-Luzgin and A. Inoue, "Nano-devitrification of glassy alloys," 2005.

[57] M. C. Gao, F. Guo, S. J. Poon, and G. J. Shiflet, "Development of fcc-Al nanocrystals in Al-Ni-Gd metallic glasses during continuous heating DSC scan," *Materials Science and Engineering A*, vol. 485, pp. 532–543, jun 2008.

[58] F. F. Han, A. Inoue, Y. Han, F. L. Kong, S. L. Zhu, E. Shalaan, F. Al-Marzouki, and A. L. Greer, "Novel Heating-Induced Reversion during Crystallization of Al-based Glassy Alloys," *Scientific Reports*, vol. 7, pp. 1–8, apr 2017.

[59] Z. Xiao, S. Yu, Y. Li, S. Ruan, L. B. Kong, Q. Huang, Z. Huang, K. Zhou, H. Su, Z. Yao, W. Que, Y. Liu, T. Zhang, J. Wang, P. Liu, D. Shen, M. Allix, J. Zhang, and D. Tang, "Materials development and potential applications of transparent ceramics: A review," jan 2020.

[60] A. A. Csontos and G. J. Shiflet, "Formation and chemistry of nanocrystalline phases formed during deformation in aluminum-rich metallic glasses," *Nanostructured Materials*, vol. 9, pp. 281–289, jan 1997.

[61] Z. P. Lu and C. T. Liu, "A new glass-forming ability criterion for bulk metallic glasses," *Acta Materialia*, vol. 50, pp. 3501–3512, aug 2002.

[62] Y. Li, S. Ng, C. Ong, H. Hng, and T. Goh, "Glass forming ability of bulk glass forming alloys," *Scripta Materialia*, vol. 36, pp. 783–787, apr 1997.

[63] A. Inoue, "Amorphous, nanoquasicrystalline and nanocrystalline alloys in Al-based systems," 1998.

[64] A. L. Greer, "Confusion by design," 1993.

[65] C. Suryanarayana and A. Inoue, *Bulk metallic glasses: Second edition.* CRC Press, jan 2017.

[66] P. K. Gupta, "Non-crystalline solids: Glasses and amorphous solids," *Journal of Non-Crystalline Solids*, vol. 195, pp. 158–164, feb 1996.

[67] V. K. Pecharsky and P. Y. Zavalij, *Fundamentals of powder diffraction and structural characterization of materials.* 2005.

[68] G. Bunker, *Introduction to XAFS.* Cambridge University Press, 2010.

[69] S. T. Chill, R. M. Anderson, D. F. Yancey, A. I. Frenkel, R. M. Crooks, and G. Henkelman, "Probing the Limits of Conventional Extended X-ray Absorption Fine Structure Analysis Using Thiolated Gold Nanoparticles," 2015.

[70] W. Mickel, S. C. Kapfer, G. E. Schröder-Turk, and K. Mecke, "Shortcomings of the bond orientational order parameters for the analysis of disordered particulate matter," *Journal of Chemical Physics*, vol. 138, p. 044501, jan 2013.

[71] F. Aurenhammer, "Voronoi diagrams—a survey of a fundamental geometric data structure," *ACM Computing Surveys (CSUR)*, vol. 23, pp. 345–405, jan 1991.

[72] Q. Du, V. Faber, and M. Gunzburger, "Centroidal Voronoi tessellations: Applications and algorithms," *SIAM Review*, vol. 41, pp. 637–676, aug 1999.

[73] G. Voronoi, "Nouvelles applications des paramètres continus à la théorie des formes quadratiques. Premier mémoire. Sur quelques propriétés des formes quadratiques positives parfaites.," *Journal für die reine und angewandte Mathematik (Crelles Journal)*, vol. 1908, no. 133, pp. 97–102, 2009.

[74] C. H. Rycroft, "VORO++: A three-dimensional Voronoi cell library in C++," 2009.

[75] P. Zhang, J. J. Maldonis, Z. Liu, J. Schroers, and P. M. Voyles, "Spatially heterogeneous dynamics in a metallic glass forming liquid imaged by electron correlation microscopy," *Nature Communications*, vol. 9, no. 1, pp. 1–7, 2018.

[76] C. J. Benmore, M. Leoni, A. O. Neto, and J. Provis, "A Review of High-Energy X-Ray Diffraction from Glasses and Liquids," *International Scholarly Research Network ISRN Materials Science*, vol. 2012.

[77] "Diamond light source." `https://www.diamond.ac.uk/`.

[78] P. Juhas, T. Davis, C. L. Farrow, and S. J. Billinge, "PDFgetX3: A rapid and highly automatable program for processing powder diffraction data into total scattering pair distribution functions," *Journal of Applied Crystallography*, 2013.

[79] S. Calvin, *XAFS for Everyone*. No. 1, 2014.

[80] J. J. Rehr and R. C. Albers, "Theoretical approaches to x-ray absorption fine structure," *Reviews of Modern Physics*, vol. 72, pp. 621–654, jul 2000.

[81] P. A. Lee, P. H. Citrin, P. Eisenberger, and B. M. Kincaid, "Extended x-ray absorption fine structure its strengths and limitations as a structural tool," *Reviews of Modern Physics*, vol. 53, pp. 769–806, oct 1981.

[82] R. L. McGreevy, "Reverse Monte Carlo modelling," 2001.

[83] O. Gereben and L. Pusztai, "RMC-POT: A computer code for reverse monte carlo modeling the structure of disordered systems containing molecules of arbitrary complexity," *Journal of Computational Chemistry*, 2012.

[84] M. I. Mendelev and M. J. Kramer, "Reliability of methods of computer simulation of structure of amorphous alloys," *Journal of Applied Physics*, vol. 107, apr 2010.

[85] M. Newville, P. Livin̦, Y. Yacoby, J. J. Rehr, and E. A. Stern, "Near-edge x-ray-absorption fine structure of Pb: A comparison of theory and experiment," *Physical Review B*, vol. 47, pp. 14126–14131, jun 1993.

[86] B. Ravel and S. D. Kelly, "The difficult chore of measuring coordination by EXAFS," in *AIP Conference Proceedings*, 2007.

[87] I. Lobzenko, Y. Shiihara, T. Iwashita, and T. Egami, "Shear Softening in a Metallic Glass: First-Principles Local-Stress Analysis," *Physical Review Letters*, vol. 124, p. 085503, feb 2020.

[88] H. Guo, P. F. Yan, Y. B. Wang, J. Tan, Z. F. Zhang, M. L. Sui, and E. Ma, "Tensile ductility and necking of metallic glass," *Nature Materials*, vol. 6, pp. 735–739, aug 2007.

[89] D. C. Hofmann, J. Y. Suh, A. Wiest, G. Duan, M. L. Lind, M. D. Demetriou, and W. L. Johnson, "Designing metallic glass matrix composites with high toughness and tensile ductility," *Nature*, vol. 451, pp. 1085–1089, feb 2008.

[90] A. Inoue and A. Takeuchi, "Recent development and application products of bulk glassy alloys," *Acta Materialia*, vol. 59, pp. 2243–2267, apr 2011.

[91] W. H. Wang, "The elastic properties, elastic models and elastic perspectives of metallic glasses," apr 2012.

[92] J. Ding and E. Ma, "Computational modeling sheds light on structural evolution in metallic glasses and supercooled liquids," dec 2017.

[93] Y. Q. Cheng, E. Ma, and H. W. Sheng, "Atomic level structure in multicomponent bulk metallic glass," *Physical Review Letters*, vol. 102, p. 245501, jun 2009.

[94] H. Wagner, D. Bedorf, S. Küchemann, M. Schwabe, B. Zhang, W. Arnold, and K. Samwer, "Local elastic properties of a metallic glass," *Nature Materials*, vol. 10, pp. 439–442, may 2011.

[95] C. A. Schuh and A. C. Lund, "Atomistic basis for the plastic yield criterion of metallic glass," jun 2003.

[96] D. Nagahama, T. Ohkubo, T. Mukai, and K. Hono, "Characterization of nanocrystal dispersed Cu/sub 60/Zr/sub 30 /Ti/sub 10/ metallic glass," *Materials Transactions*, vol. 46, no. 6, pp. 1264–1270, 2005.

[97] R. B. Dandliker, R. D. Conner, and W. L. Johnson, "Melt infiltration casting of bulk metallic-glass matrix composites," *Journal of Materials Research*, vol. 13, no. 10, pp. 2896–2901, 1998.

[98] T. Demirtaş and Y. E. Kalay, "Kinetics of fcc-Al nanocrystallization in Al90Tb10 metallic glass," *Journal of Non-Crystalline Solids*, 2013.

[99] J. H. Perepezko, R. J. Hebert, R. I. Wu, and G. Wilde, "Primary crystallization in amorphous Al-based alloys," in *Journal of Non-Crystalline Solids*, 2003.

[100] D. R. Allen, J. C. Foley, and J. H. Perepezko, "Nanocrystal development during primary crystallization of amorphous alloys," *Acta Materialia*, 1998.

[101] W. G. Stratton, J. Hamann, J. H. Perepezko, P. M. Voyles, X. Mao, and S. V. Khare, "Aluminum nanoscale order in amorphous Al92 Sm8 measured by fluctuation electron microscopy," *Applied Physics Letters*, 2005.

[102] G. Wilde, H. Sieber, and J. Perepezko, "Glass formation versus nanocrystallization in an Al92Sm8alloy," *Scripta Materialia*, 1999.

[103] A. K. Gangopadhyay, T. K. Croat, and K. F. Kelton, "Effect of phase separation on subsequent crystallization in Al88Gd6La2Ni4," *Acta Materialia*, 2000.

[104] T. K. Croat, A. K. Gangopadhyay, and K. F. Kelton, "Crystallization in Al88Re8Ni4 glass-forming alloys," *Philosophical Magazine A: Physics of Condensed Matter, Structure, Defects and Mechanical Properties*, 2002.

[105] K. K. Sahu, N. A. Mauro, L. Longstreth-Spoor, D. Saha, Z. Nussinov, M. K. Miller, and K. F. Kelton, "Phase separation mediated devitrification of Al88Y 7Fe5 glasses," *Acta Materialia*, 2010.

[106] K. Hono, D. H. Ping, M. Ohnuma, and H. Onodera, "Cu clustering and Si partitioning in the early crystallization stage of an Fe73.5Si13.5B9Nb3Cu1 amorphous alloy," *Acta Materialia*, vol. 47, no. 3, pp. 997–1006, 1999.

[107] K. Kajiwara, M. Ohnuma, T. Ohkubo, D. H. Ping, and K. Hono, "APFIM/TEM/SAXS studies of early stage crystallization of a Zr52.5Cu17.9Ni14.6Al10Ti5 metallic glass," *Materials Science and Engineering A*, vol. 375-377, pp. 738–743, jul 2004.

[108] M. Ovun, M. Kramer, and Y. Kalay, "Structural modeling of liquid and amorphous Al91Tb9 by Monte Carlo simulations," *Journal of Non-Crystalline Solids*, 2014.

[109] C. Yildirim, M. Kutsal, R. T. Ott, M. F. Besser, M. J. Kramer, and Y. E. Kalay, "The role of amorphous precursor in phase selection hierarchy in marginal metallic glasses," *Materials and Design*, vol. 112, pp. 479–484, dec 2016.

[110] B. Ravel and M. Newville, "ATHENA, ARTEMIS, HEPHAESTUS: Data analysis for X-ray absorption spectroscopy using IFEFFIT," in *Journal of Synchrotron Radiation*, 2005.

[111] A. Savitzky and M. J. Golay, "Smoothing and Differentiation of Data by Simplified Least Squares Procedures," *Analytical Chemistry*, 1964.

[112] O. Gereben, P. Jóvári, L. Temleitner, and L. Pusztai, "A new version of the RMC++ Reverse Monte Carlo programme, aimed at investigating the structure of covalent glasses," in *Journal of Optoelectronics and Advanced Materials*, 2007.

[113] G. Voronoi, "Nouvelles applications des paramètres continus à la théorie des formes quadratiques. Deuxième mémoire. Recherches sur les parallélloèdres primitifs.," *Journal fur die Reine und Angewandte Mathematik*, 1908.

[114] H. E. Kissinger, "Reaction Kinetics in Differential Thermal Analysis," *Analytical Chemistry*, 1957.

[115] T. Ozawa, "A New Method of Analyzing Thermogravimetric Data," *Bulletin of the Chemical Society of Japan*, vol. 38, pp. 1881–1886, nov 1965.

[116] H. Y. Hsieh, T. Egami, Y. He, S. J. Poon, and G. J. Shiflet, "Short range ordering in amorphous Al90FexCe10-x," *Journal of Non-Crystalline Solids*, 1991.

[117] W. K. Luo and E. Ma, "EXAFS measurements and reverse Monte Carlo modeling of atomic structure in amorphous Ni80P20 alloys," *Journal of Non-Crystalline Solids*, 2008.

[118] T. Q. Wen, Y. Zhang, C. Z. Wang, N. Wang, K. M. Ho, and M. J. Kramer, "Local structure orders and glass forming ability of Ni-Nb liquids," *Intermetallics*, vol. 98, pp. 131–138, jul 2018.

[119] J. J. Rehr, J. J. Kas, F. D. Vila, M. P. Prange, and K. Jorissen, "Parameter-free calculations of X-ray spectra with FEFF9," jun 2010.

[120] R. V. Gumeniuk, B. M. Stel'makhovych, and Y. B. Kuz'ma, "The Tb-Ag-Al system," *Journal of Alloys and Compounds*, vol. 321, pp. 132–137, may 2001.

[121] R. Bacewicz and J. Antonowicz, "XAFS study of amorphous Al-RE alloys," *Scripta Materialia*, vol. 54, pp. 1187–1191, mar 2006.

[122] P. Malet, M. J. Capitan, M. A. Centeno, J. A. Odriozola, and I. Carrizosa, "EXAFS data analysis for lanthanide sesquioxides," *Journal of the Chemical Society, Faraday Transactions*, vol. 90, no. 18, pp. 2783–2790, 1994.

[123] R. Anderson, T. Brennan, G. Mountjoy, R. J. Newport, and G. A. Saunders, "An EXAFS study of rare-earth phosphate glasses in the vicinity of the metaphosphate composition," *Journal of Non-Crystalline Solids*, vol. 232-234, pp. 286–292, jul 1998.

[124] D. Bowron, G. Saunders, R. Newport, B. Rainford, and H. Senin, "EXAFS studies of rare-earth metaphosphate glasses," *Physical Review B - Condensed Matter and Materials Physics*, vol. 53, no. 9, pp. 5268–5275, 1996.

[125] M. Liu and R. Y. Wang, "Size-dependent melting behavior of colloidal in, Sn, and Bi nanocrystals," *Scientific Reports*, vol. 5, pp. 1–9, nov 2015.

[126] C. A. Schuh, T. C. Hufnagel, and U. Ramamurty, "Mechanical behavior of amorphous alloys," *Acta Materialia*, vol. 55, pp. 4067–4109, jul 2007.

[127] Y. Yang, J. C. Ye, J. Lu, F. X. Liu, and P. K. Liaw, "Effects of specimen geometry and base material on the mechanical behavior of focused-ion-beam-fabricated metallic-glass micropillars," *Acta Materialia*, vol. 57, pp. 1613–1623, mar 2009.

[128] J. C. Ye, J. Lu, Y. Yang, and P. K. Liaw, "Extraction of bulk metallic-glass yield strengths using tapered micropillars in micro-compression experiments," *Intermetallics*, vol. 18, pp. 385–393, mar 2010.

[129] R. Maaß, S. Van Petegem, D. Ma, J. Zimmermann, D. Grolimund, F. Roters, H. Van Swygenhoven, and D. Raabe, "Smaller is stronger: The effect of strain hardening," 2009.

[130] G. Kumar, A. Desai, and J. Schroers, "Bulk metallic glass: The smaller the better," *Advanced Materials*, vol. 23, pp. 461–476, jan 2011.

[131] Z. Ye, F. Meng, F. Zhang, Y. Sun, L. Yang, S. H. Zhou, R. E. Napolitano, M. I. Mendelev, R. T. Ott, M. J. Kramer, C. Z. Wang, and K. M. Ho, "Observation of η-Al41Sm5 reveals motif-aware structural evolution in Al-Sm alloys," *Scientific Reports*, vol. 9, p. 6692, dec 2019.

[132] M. E. Gurtin, "On the plasticity of single crystals: Free energy, microforces, plastic-strain gradients," *Journal of the Mechanics and Physics of Solids*, vol. 48, pp. 989–1036, may 2000.

[133] P. Thamburaja and R. Ekambaram, "Coupled thermo-mechanical modelling of bulk-metallic glasses: Theory, finite-element simulations and experimental verification," *Journal of the Mechanics and Physics of Solids*, vol. 55, pp. 1236–1273, jun 2007.

[134] P. Thamburaja, "Length scale effects on the shear localization process in metallic glasses: A theoretical and computational study," *Journal of the Mechanics and Physics of Solids*, vol. 59, pp. 1552–1575, aug 2011.